Nano Research

Open Access

Research Article

cCLT1-decorated nanodisk as a novel cancer-associated fibroblast-targeted curcumin delivery system for enhanced breast tumor metastasis treatment by TME remodeling

Chuchu Zhou[1,2], Shangshang Xiong[1], Mingzhu Cai[1], Xiaoxi Yang[1,2], Jing Wei[1,2], Qian Chen[1,2], and Peng Guo[1,2] ✉

[1] *Clinical Research Center, Beijing Children's Hospital, Capital Medical University, National Center for Children's Health, Beijing 100045, China*

[2] *Key Laboratory of Major Diseases in Children, Ministry of Education, Beijing Children's Hospital, Capital Medical University, National Center for Children's Health, Beijing 100045, China*

Cite this article: *Nano Research*, **2026**, *19*, 94908905. https://doi.org/10.26599/NR.2026.94908905

ABSTRACT: Breast cancer remains one of the leading causes of cancer-related mortality in women, with metastasis being the primary driver of treatment failure and poor prognosis. Multiple components within the tumor microenvironment (TME) work together to promote tumor metastasis, among which cancer-associated fibroblasts (CAFs) function as the central mediators of tumor-stroma crosstalk. In this study, we fabricated a novel nanodisk-based platform for curcumin (CUR) delivery to selectively suppress CAF activation. By functionalizing nanodisks (NDs) with the cyclic peptide CGLIIQKNEC (cCLT1), the resulting formulation (ND/P-CUR) enabled preferential CUR delivery to CAFs. Benefiting from both the structural advantages of NDs and the specific affinity of cCLT1 toward cellular fibronectin (cFN), ND/P-CUR effectively promoted CAF reprogramming and TME remodeling. Mechanistic investigations revealed that ND/P-CUR markedly reduced extracellular matrix (ECM) deposition, downregulated transforming growth factor-beta 1 (TGF-β1) expression, and suppressed tumor angiogenesis, thereby enhancing the inhibition of tumor growth and metastatic progression. Collectively, this CAF-targeted TME remodeling strategy based on cCLT1-functionalized NDs represents a promising therapeutic approach for breast cancer, and is expected to be applicable to the treatment of other stroma-rich tumors.

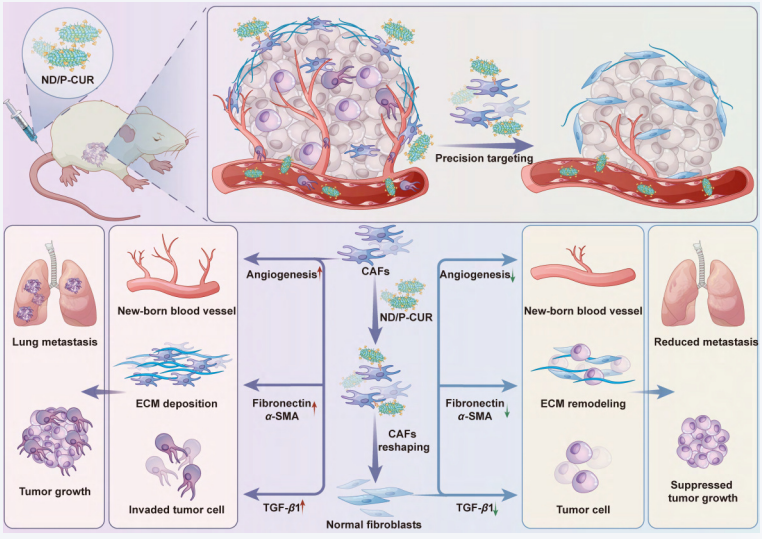

KEYWORDS: breast cancer, metastasis inhibition, cyclic peptide CGLIIQKNEC (cCLT1)-functionalized nanodisks, cancer-associated fibroblast (CAF) reprogramming, tumor microenvironment (TME) remodeling

1 Introduction

Breast cancer is one of the most prevalent malignancies and a leading cause of cancer-related mortality in women worldwide [1]. Although substantial advancements in diagnosis and multimodal therapies have improved clinical outcomes for early-stage breast cancer [2, 3], metastasis involved in the advanced stages is still difficult to control and accounts for most treatment failures [4–7]. Therefore, the development of effective therapies capable of suppressing both primary tumor growth and metastatic progression is urgently needed.

Nanotechnology-based drug delivery systems have emerged as promising strategies to improve therapeutic outcomes by modulating drug pharmacokinetics, biodistribution, and cellular uptake [8]. Among the key physicochemical features of

Received: March 12, 2026; **Revised:** May 31, 2026
Accepted: June 2, 2026

✉Address correspondence to guopeng@bch.com.cn

nanocarriers, particle shape has been recognized as a critical determinant of the *in vivo* biological behaviors [9, 10]. Disk-shaped nanoparticles (nanodisks, NDs) have attracted increasing interest owing to their distinctive anisotropic geometry [11]. NDs are spontaneously assembled when polyethylene glycol (PEG)ylated lipids exceed a critical molar ratio of 15%, resulting in a flat discoidal lipid bilayer stabilized by PEG chains along the rim [11]. Compared with conventional nanospheres, this unique morphology endows NDs with several advantages, including enhanced cellular internalization, prolonged circulation time, and improved vascular margination [12–15]. Previous studies have demonstrated the potential of NDs as drug carriers in biomedical applications [16]. For example, melittin-loaded NDs showed superior antibacterial efficacy in comparison to free melittin, highlighting the contribution of disk-like geometry to therapeutic performance [17, 18]. Additionally, NDs displayed sustained drug release and improved penetration within solid tumors, suggesting their promise in cancer therapy [19]. Motivated by these shape-dependent characteristics, we employed NDs as the delivery platform for curcumin (CUR) to investigate their potential in enhancing antitumor and antimetastatic efficacy against breast cancer.

Although NDs provide favorable shape advantages for passive targeting, relying on passive accumulation alone is often insufficient for expected therapeutic outcomes. Therefore, proper ligands should be decorated on the nanocarrier surface to further achieve active targeting. Traditional cancer therapies primarily focus on targeting tumor cells [20–22], while ignoring the malignant interactions among multiple components within the tumor microenvironment (TME), which provides both structural support and biochemical cues that facilitate tumor invasion and metastasis [23–25]. Among the stromal components, cancer-associated fibroblasts (CAFs) serve as central regulators of tumor-stroma crosstalk and promote tumor progression through induction of pathological angiogenesis, excessive deposition of extracellular matrix (ECM), and secretion of pro-tumorigenic cytokines [23, 26–33]. Therefore, developing a CAF-targeted delivery system to induce CAF reprogramming represents a desirable strategy for suppressing tumor progression and metastasis.

Fibronectin (FN) exists in two major forms based on its solubility, including soluble disulfide-bonded dimeric plasma fibronectin (pFN) and insoluble cellular fibronectin (cFN) present on the cell surface or in the ECM [34–36]. In the tumor stroma of breast cancer, cFN is highly expressed on activated CAFs and abundantly deposited within the ECM, which has been widely recognized as a mesenchymal marker that aids in the identification of CAFs [37–39]. Moreover, cFN is minimally present in most normal tissues, making it an ideal target for CAF-targeted therapeutic strategies. Previous studies have reported that the cyclic peptide CGLIIQKNEC (cCLT1) preferentially recognizes cFN in the tumor stroma and has been applied in the cancer molecular imaging with magnetic resonance imaging (MRI) [40–44]. However, its potential for targeting CAFs in breast cancer, particularly in the context of CAF-targeted nanodrug delivery systems, has yet to be fully explored.

Herein, we developed a CAF-targeted nanodisk-based delivery system to suppress the growth and metastasis of breast cancer. CUR, a natural polyphenol with broad anti-inflammatory and antitumor activity, was encapsulated into NDs, followed by surface decoration of cCLT1 to generate the final CAF-targeted nanoplatform (ND/P-CUR). We hypothesized that by integrating the shape-dependent delivery advantages of NDs with cCLT1-mediated recognition of cFN, ND/P-CUR could efficiently deliver CUR to CAFs, thereby promoting CAF reprogramming and subsequent TME remodeling. We systematically evaluated the targeting ability, therapeutic efficacy, and the underlying mechanisms of ND/P-CUR both *in vitro* and *in vivo*. This study aims to provide a reference for the development of CAF-targeted nanotherapeutic strategies against breast cancer progression and metastasis.

2 Experimental

2.1 Materials

Hydrogenated soy phosphatidylcholine (HSPC), 1,2-distearoyl-*sn*-glycero-3-phosphoethanolamine-N-amino(polyethylene glycol)-2000 and cholesterol were obtained from AVT Pharmaceutical Tech Co., Ltd. (Shanghai, China). Curcumin and 1,1'-dioctadecyl-3,3,3',3'-tetramethylindocarbocyanine perchlorate (DiD) were acquired from Yuanye Biotechnology Co., Ltd. (Shanghai, China). Amicon® Ultra centrifugal filter devices were purchased from Merck Millipore. The cCLT1 was synthesized by Qiangyao Biotechnology Co., Ltd. (Shanghai, China). Bovine pFN and human cFN were obtained from Ethephon Biotechnology Co., Ltd. (Shanghai, China). D-Luciferin potassium was purchased from Meilun Biotechnology Co., Ltd. (Dalian, China). All other chemicals were obtained from commercial sources.

2.2 Animals and cell culture

Mouse embryonic fibroblasts (NIH-3T3) were cultured in Dulbecco's modified Eagle's medium (DMEM; Gibco, USA), supplemented with 10% fetal bovine serum (FBS; Gibco, USA), 100 U/mL Penicillin, and 100 μg/mL Streptomycin (Solarbio, Beijing, China). Murine breast cancer cells (4T1) and luciferase-transferred 4T1 cells (4T1-luc) were cultured in RPMI 1640 medium (HyClone, Logan, UT, USA) with the same supplements. Female BALB/c mice (6–8 weeks) were purchased from the SiPeiFu Biotechnology Co., Ltd. (Beijing, China). All animal experiments were conducted following the institutional guidelines and approved by the Animal Ethics Committee of the Institute of Materia Medica, Chinese Academy of Medical Sciences and Peking Union Medical College (approval number: 00008419).

2.3 Synthesis of DSPE-PEG2000-cCLT1

DSPE-PEG2000-cCLT1 was synthesized through the reaction between the amino group (–NH_2) of cysteine residue in cCLT1 peptide and the carboxyl group (–COOH) of DSPE-PEG2000-COOH as previously described [45]. Briefly, the fluorenylmethyloxycarbonyl (Fmoc)-protected-CLT1 linear peptide was first synthesized by solid-phase peptide synthesis (SPPS) method. DSPE-PEG2000-COOH was then dissolved in dimethylformamide (DMF), followed by the addition of Fmoc-protected-CLT1 linear peptide at a molar ratio of 3:1 (DSPE-PEG2000-COOH: Fmoc-protected-CLT1 linear peptide). Subsequently, the reaction system was stirred at room temperature for 24 h, followed by deprotection and cyclization. The resulting product was dialyzed (molecular weight cutoff (MWCO) = 3500 Da) for 48 h and lyophilized for an additional 24 h. Successful conjugation of DSPE-PEG2000-cCLT1 was confirmed by matrix-assisted laser desorption/ionization time-of-flight mass spectrometry (MALDI-TOF MS) (AB SCIEX, USA)

and Fourier-transform infrared spectroscopy (FTIR) (Thermo Electron Corporation, USA).

2.4 Preparation of nanodisks

Nanodisks (NDs) were prepared by the thin-film hydration method. Briefly, HSPC, cholesterol, DSPE-PEG2000 and curcumin (CUR) were dissolved in chloroform at a molar ratio of 4:5:3:2 in a round-bottom flask. The organic solvent was removed by rotary evaporation at 37 °C for 30 min to form a uniform lipid film. Subsequently, 10 mL of phosphate-buffered saline (PBS) was added to fully hydrate the lipid film. The resulting dispersion was sonicated at 150 W for 20 min in an ice bath. Finally, the suspension was filtered through a 0.22 μm polyethersulfone (PES) membrane to obtain the CUR-loaded nanodisks (ND-CUR). For the preparation of ND-CUR decorated with peptide cCLT1 (ND/P-CUR), the same procedure was followed, except that DSPE-PEG2000 was replaced with a mixture of DSPE-PEG2000 and DSPE-PEG2000-cCLT1. Nanospheres (NSs) were prepared using the same method as NDs, but with a different molar ratio of 7:7:1:2 for HSPC, cholesterol, DSPE-PEG2000, and CUR. The lipid film was hydrated, sonicated, and then filtered to obtain CUR-loaded NSs (NS-CUR). For DiD-labeled NDs and NSs, including ND-DiD, NS-DiD and ND/P-DiD, the mass ratio of DiD to total lipid was adjusted to 1:125.

2.5 Characterizations of nanodisks

The particle size, polydispersity index (PDI), and zeta potential of NS-CUR, ND-CUR and ND/P-CUR were measured using Malvern Zetasizer (Nano ZS90, Malvern Panalytical, UK) at 25 °C. The morphology of the NDs was observed under transmission electron microscopy (TEM; JEM-1400Plus, JEOL Ltd., Japan) using the negative staining method. Additionally, atomic force microscopy (AFM; Bruker, USA) was employed to determine the height profile of ND/P-CUR. To evaluate the stability of the NDs, the obtained formulations were stored at 4 °C, and changes in particle size distribution were monitored within 14 days.

The drug loading capacity (DL) and encapsulation efficiency (EE) were determined by the ultrafiltration method. Briefly, 0.5 mL of NS-CUR, ND-CUR or ND/P-CUR was loaded into an Amicon® Ultra centrifugal filter device (MWCO: 10 kDa) and centrifuged at 5000*g* for 30 min. After centrifugation, the free drug passed through the membrane, while the drug-loaded nanoparticles (NPs) were retained in the filtration unit. The concentration of free CUR in the filtrate was quantified by high-performance liquid chromatography (HPLC), and the amount of encapsulated CUR was calculated by subtracting the free CUR concentration from the initial total drug concentration. The DL and EE were calculated using the following equations (Eqs. (1) and (2)):

$$\mathrm{DL}\% = \frac{\text{Weight of encapsulated CUR}}{\text{Total weight of NPs}} \times 100\% \quad (1)$$

$$\mathrm{EE}\% = \frac{\text{Weight of encapsulated CUR}}{\text{Total weight of CUR}} \times 100\% \quad (2)$$

In vitro drug release was performed using the dialysis method. Briefly, samples (1 mL) of free CUR, NS-CUR, ND-CUR, and ND/P-CUR were individually loaded into respective dialysis bags (MWCO: 8000 Da). The bags were then immersed in 40 mL of PBS containing 0.2% Tween 80 (v/v) to maintain sink conditions, and incubated at 37 °C with gentle agitation. At predetermined time points, 1.0 mL of the release medium was withdrawn and immediately replaced with an equivalent volume of fresh buffer. The collected samples were diluted with ethanol, and the concentration of CUR was quantified via HPLC.

2.6 Cellular uptake

The cellular uptake study was performed to evaluate the *in vitro* targeting capability of cCLT1-decorated NDs in TGF-β1-activated NIH-3T3 cells. Briefly, NIH-3T3 cells were seeded at an appropriate density and allowed to adhere for 24 h at 37 °C. The culture medium was then replaced with fresh medium containing 10 ng/mL TGF-β1 to induce the cells into CAF phenotype [46]. Subsequently, fresh medium containing NS-DiD, ND-DiD, or ND/P-DiD at an equivalent DiD concentration of 100 ng/mL was separately added. Following 4 h of incubation, the cells were washed three times with PBS. For qualitative observation, cells cultured in confocal dishes were fixed with 4% paraformaldehyde for 15 min at room temperature and stained with 4',6-diamidino-2-phenylindole (DAPI). The intracellular distribution of DiD was observed using a confocal laser scanning microscope (CLSM) (Leica, Germany). For quantitative analysis, cells cultured in 6-well plates were subjected to the same treatments, harvested and analyzed by flow cytometry (BD Biosciences, USA). To further verify that the cellular uptake was mediated by cCLT1, a competitive blocking study was conducted in parallel. Briefly, adherent cells were pretreated with free cCLT1 peptide for 1 h prior to incubation with ND/P-DiD, followed by the same procedures described above.

To confirm the selective CAF-targeting behavior of ND/P-DiD, 4T1 cells and quiescent NIH-3T3 fibroblasts were also used for cellular uptake studies. The cells were treated with NS-DiD, ND-DiD, or ND/P-DiD at the same DiD concentration and incubation time as described above, followed by flow cytometric analysis. For the blocking group, cells were pretreated with free cCLT1 peptide for 1 h before ND/P-DiD incubation.

2.7 *In vitro* validation of cFN recognition by ND/P-CUR

In this study, we performed *in vitro* experiments to validate the specific recognition of cFN by ND/P-CUR and to demonstrate whether pFN interferes with this targeting behavior.

First, the plasma stability assay was conducted to evaluate whether soluble plasma components, including pFN, affected the colloidal stability of ND/P-CUR in plasma [47]. Briefly, ND/P-CUR was diluted 10-fold with rat plasma and incubated at 37 °C. At predetermined time points, changes in particle size and PDI were monitored and recorded.

To directly verify the specific recognition of cFN by ND/P-CUR, a competitive uptake study with pFN and cFN was performed. ND/P-DiD was preincubated with pFN, cFN, bovine serum albumin (BSA), or PBS at 37 °C for 60 min before incubation with CAFs. BSA was employed as a nonspecific protein control. After preincubation, the different ND/P-DiD formulations were added to CAFs. The following procedures, including cellular incubation, washing, harvesting, and flow cytometry analysis, were performed as described in Section 2.6.

2.8 *In vitro* cytotoxicity

Cell viability was assessed by an 3-(4,5-dimethylthiazol-2-yl)-2,5-diphenyltetrazolium bromide (MTT) assay in TGF-β1-activated NIH-3T3 cells. Briefly, NIH-3T3 cells were seeded into 96-well plates and cultured overnight. On the next day, free CUR, NS-CUR,

ND-CUR, or ND/P-CUR at an equivalent CUR concentration were added to the culture medium supplemented with 10 ng/mL TGF-β1. Cells incubated with 10 ng/mL TGF-β1 alone served as the control group. After 24 h, MTT solution was added to each well, and the cells were further incubated for 4 h. The culture medium was then carefully removed, followed by the addition of dimethyl sulfoxide (DMSO) to dissolve the formazan crystals. The absorbance was measured at 490 nm using a microplate reader (Bio-Tek Instruments, Inc., USA). To further evaluate the biosafety of different formulations, parallel experiments were conducted in quiescent NIH-3T3 cells under identical treatment conditions but in the absence of TGF-β1 stimulation. Cell viability was calculated according to the following equation, in which A(sample), A(control) and A(blank) represent the absorbance values of treated cells, control cells, and blank wells, respectively (Eq. (3)):

$$\text{Cell viability}\ (\%) = \frac{A(\text{sample}) - A(\text{blank})}{A(\text{control}) - A(\text{blank})} \times 100\% \qquad (3)$$

2.9 Suppression of CAF activation

The alpha-smooth muscle actin (α-SMA) expression level in TGF-β1-activated NIH-3T3 cells was examined to evaluate the effects of different formulations on cellular activation. After overnight attachment, NIH-3T3 cells were treated with PBS, free CUR, NS-CUR, ND-CUR or ND/P-CUR at an equivalent CUR concentration in the presence of TGF-β1 (10 ng/mL) for 24 h. For immunofluorescence analysis, the cells were fixed and permeabilized, followed by blocking with 5% bovine serum albumin for 1 h. The cells were then incubated with anti-α-SMA primary antibody at 4 °C overnight. After thorough washing, AF488-conjugated secondary antibody was applied, and nuclei were counterstained with DAPI. Fluorescence images were captured using a confocal laser scanning microscope (Leica, Germany).

In parallel, α-SMA expression was further examined at the protein level by Western blotting (WB) analysis. The collected cells were lysed with radioimmunoprecipitation assay (RIPA) buffer supplemented with protease inhibitors. After measuring the total protein concentration by the bicinchoninic acid (BCA) assay kit, equal amounts of protein were separated by sodium dodecyl sulfate-polyacrylamide gel electrophoresis (SDS-PAGE) and transferred onto polyvinylidene difluoride (PVDF) membranes. The membranes were then blocked in 5% nonfat milk, and incubated with primary antibody against α-SMA at 4 °C overnight, followed by horseradish peroxidase (HRP)-conjugated secondary antibody. Protein bands were visualized using an enhanced chemiluminescence imaging system (Clinx Science Instruments, China).

Additionally, FN, SMAD3, and phosphorylated SMAD3 (p-SMAD3) were examined by WB using the same procedure to further evaluate the inhibitory effect of different formulations on CAF activation and the potential involvement of the TGF-β/SMAD family member 3 (SMAD3) signaling pathway.

2.10 *In vitro* cell migration assay

Given that metastasis is a major cause of treatment failure and mortality in breast cancer, an *in vitro* cell migration assay was performed to evaluate the antimetastatic efficacy of ND/P-CUR. Briefly, TGF-β1-activated NIH-3T3 cells were treated with PBS (control), free CUR, NS-CUR, ND-CUR, or ND/P-CUR at an equivalent CUR concentration. The conditioned medium (CM) was collected, filtered to remove cell debris, and used for the subsequent wound healing assay. 4T1 cells were seeded into 6-well plates and cultured until reaching approximately 90%–100% confluence. A linear wound was then scratched across the cell monolayer using a sterile 200 μL pipette tip. Detached cells were gently removed by washing twice with PBS, followed by the addition of the collected CM. Images of the wounded areas were captured at 0 and 24 h using an inverted optical microscope. The wound healing rate was quantified by measuring the wound area and calculated to assess antimetastatic efficacy [48].

2.11 Tumor spheroid formation and imaging

Multicellular tumor spheroids (MCTs) penetration assay was performed to evaluate the penetration ability of NDs *in vitro*. The MCTs were established by co-culturing 4T1 cells with TGF-β1-activated NIH-3T3 cells (4T1 cells: TGF-β1-activated NIH-3T3 cells = 2:1) using the hanging drop method and allowed to grow for 3 days. The spheroids were then carefully transferred to culture wells and incubated for another 3 days prior to treatment. Subsequently, the spheroids were incubated with NS-DiD, ND-DiD or ND/P-DiD at an equivalent DiD concentration in serum-free medium for 4 h. After incubation, the spheroids were gently washed twice with PBS to remove free formulations and then fixed with 4% paraformaldehyde. The intratumoral distribution of the formulations within the spheroids was visualized by confocal laser scanning microscopy (Leica, Germany). Z-stack images were acquired at defined intervals along the *z*-axis, and fluorescence intensity profiles were quantified to assess the penetration depth.

2.12 Biodistribution study

Female BALB/c mice bearing orthotopic breast tumors were established by injecting the mixed cell suspension containing 4T1 (1×10^6) cells and NIH-3T3 (5×10^5) cells into the right mammary fat pad [49]. When the tumor volume reached approximately 400 mm^3, the tumor-bearing mice were randomly assigned to four groups and intravenously administered with free DiD, NS-DiD, ND-DiD, or ND/P-DiD, respectively. At predetermined time points after injection, the mice were sacrificed and major organs were excised. The collected tissues were rinsed with saline to remove residual blood and subjected to *ex vivo* fluorescence imaging using an *in vivo* imaging system (Caliper-Perkin Elmer, USA). Regions of interest (ROI) were defined for each organ, and the fluorescence intensity within each ROI was further semi-quantified to evaluate the biodistribution profiles of different formulations.

2.13 *In vivo* therapeutic efficacy

To establish an orthotopic breast tumor model for antitumor efficacy evaluation, 1×10^6 luciferase-transferred 4T1 cells (4T1-luc) and 5×10^5 NIH-3T3 cells were injected into the right mammary fat pad of BALB/c mice [49]. On day 9 after inoculation, the tumor-bearing BALB/c mice were randomly assigned to five groups ($n = 6$ per group) and intravenously administered saline, free CUR, NS-CUR, ND-CUR, or ND/P-CUR, respectively. The treatment frequency was every 2 days for a total of 4 doses. Throughout the treatment period, body weight and tumor volume of the mice were recorded at predetermined intervals. Tumor volume was calculated using the standard equation (Eq. (4)):

$$V = \frac{\text{Length} \times \text{Width}^2}{2} \quad (4)$$

On day 29 post-inoculation, mice were intraperitoneally injected with D-luciferin potassium salt and euthanized 15 min later. Tumors were harvested and weighed for further analysis. A portion of the tumors was fixed in 4% paraformaldehyde, embedded in paraffin, and sectioned for histological examination. Hematoxylin and eosin (H&E) staining was performed to evaluate tumor morphology, and immunohistochemical staining for CD31 was conducted to assess tumor angiogenesis. The remaining excised tumors were homogenized, and the expression levels of specific proteins were analyzed by Western blotting according to standard protocols. Additionally, the lungs and other major organs were also carefully excised, washed with PBS, and subjected to bioluminescence imaging by an *in vivo* imaging system (Caliper-Perkin Elmer, USA). H&E staining of the lungs was also conducted to further evaluate the antimetastatic efficacy of ND/P-CUR.

2.14 Statistical analysis

All data were expressed as mean ± standard deviation (SD) and passed the Shapiro-Wilk normality test. Statistical comparisons between multiple groups were performed using one-way analysis of variance (ANOVA) with Tukey's test for pairwise comparisons. $P < 0.05$ was considered statistically significant.

3 Results

3.1 Synthesis of DSPE-PEG2000-cCLT1

cCLT1 can preferentially recognize cFN, which is highly expressed on activated CAFs and abundantly deposited within the ECM. Hence, cCLT1 was selected as the targeting ligand and modified on the surface of NDs. For precise control of ligand density, cCLT1 was first conjugated with DSPE-PEG2000-COOH via the reaction between the amino group ($-NH_2$) of cysteine residue in cCLT1 peptide and the carboxy group (–COOH) in DSPE-PEG2000-COOH (Fig. S1 in the Electronic Supplementary Material (ESM)). The successful synthesis of DSPE-PEG2000-cCLT1 was confirmed by MALDI-TOF-MS (Fig. 1(g)). According to the certificate of analysis (COA) for DSPE-PEG2000-COOH, its molecular weight

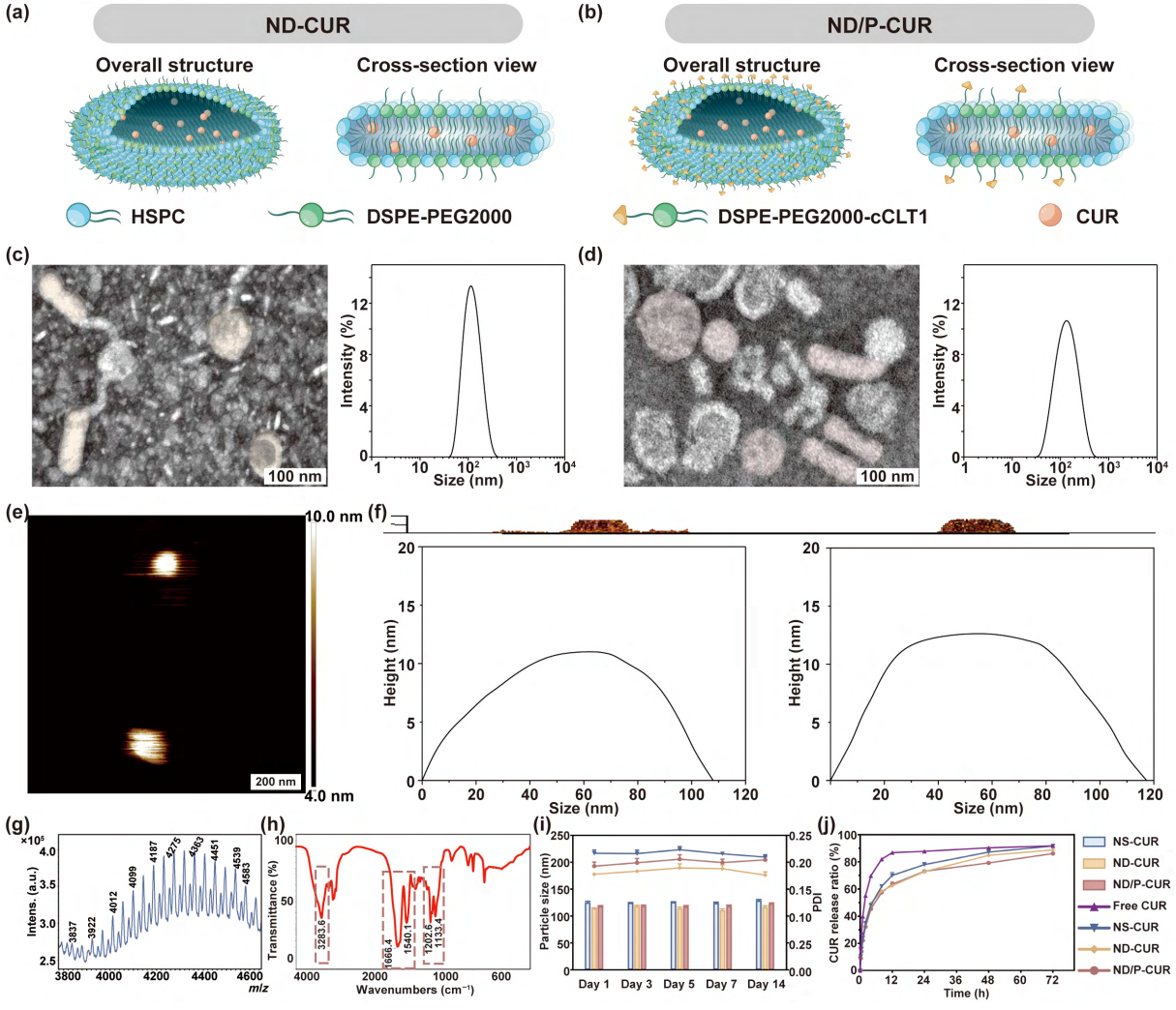

Figure 1 Characterization of ND-CUR and ND/P-CUR. Schematic illustrations of the overall structures and cross-section views of (a) ND-CUR and (b) ND/P-CUR. Representative TEM images and corresponding particle size distributions of (c) ND-CUR and (d) ND/P-CUR. (e) AFM images of ND/P-CUR from top view. (f) AFM images of ND/P-CUR from side view and height profiles of the two individual particles. Successful synthesis of DSPE-PEG2000-cCLT1 was confirmed by (g) MALDI-TOF MS and (h) FTIR spectroscopy. (i) *In vitro* stability of NS-CUR, ND-CUR, and ND/P-CUR at 4 °C for 14 days. (j) Cumulative CUR release profiles of free CUR, NS-CUR, ND-CUR, and ND/P-CUR in PBS containing 0.2% Tween 80 over 72 h. Data are presented as mean ± SD ($n = 3$).

varied from 2900 to 3300 Da due to the polydispersity of PEG chain. MALDI-TOF-MS results showed that the average molecular weight of DSPE-PEG2000-cCLT1 ranged from 4000 to 4400 Da, approximately 1100 Da higher than that of DSPE-PEG2000-COOH, which was consistent with the molecular weight of cCLT1 peptide. In addition, the characteristic FTIR peaks observed at 3283, 1666, and 1540 cm^{-1}, along with additional peaks at 1202 and 1133 cm^{-1}, corresponding to the amido group and ether group, respectively, further verified the conjugation between cCLT1 and DSPE-PEG2000-COOH (Fig. 1(h) and Fig. S2 in the ESM).

3.2 Preparation and characterizations of nanodisks

The nanodisks were successfully prepared using the thin-film hydration method. The particle size and zeta potential of ND-CUR and ND/P-CUR were measured by dynamic light scattering (DLS). As summarized in Table S1 in the ESM, the average particle size of ND-CUR was measured to be approximately 114.4 ± 3.8 nm, with a PDI of 0.178 ± 0.030 (Fig. 1(c)), indicating a narrow size distribution. ND/P-CUR exhibited a similar particle size of 118.5 ± 4.1 nm and a PDI of 0.193 ± 0.032 (Fig. 1(d)). The zeta potential of ND-CUR was −18.6 ± 2.3 mV, while ND/P-CUR exhibited a slightly more negative zeta potential of −20.1 ± 2.5 mV, suggesting good colloidal stability.

The morphology of ND-CUR and ND/P-CUR was subsequently examined by transmission electron microscopy (TEM). TEM images (Figs. 1(c) and 1(d)) revealed a mixture of rod-like and spherical structures, corresponding to different orientations of the NDs (Figs. 1(a) and 1(b)). Specifically, the rod-like structures represented the cross-section view of the NDs, whereas the spherical structures represented the vertical-section view, confirming the successful fabrication of NDs with a typical disk-like morphology. AFM analysis further supported the above interpretation. As shown in Figs. 1(e) and 1(f), both the topographic view and the corresponding height profiles of representative particles were obtained. ND/P-CUR exhibited an average height of 11.5 ± 0.7 nm and an approximate lateral diameter of 115 nm (Fig. 1(f)), which was generally consistent with the hydrodynamic size determined by DLS and the morphological observations from TEM. The DL and EE were quantitatively determined using the ultrafiltration method. As shown in Table S1 in the ESM, ND-CUR exhibited a DL of 5.49% ± 0.27% and an EE of 83.5% ± 1.7%. Similarly, ND/P-CUR showed a comparable DL of 5.24% ± 0.45% and an EE of 82.7% ± 3.1%, demonstrating efficient encapsulation of CUR in both formulations. The physical stability of the NDs was assessed by monitoring changes in particle size and PDI over time. Both ND-CUR and ND/P-CUR exhibited relatively constant particle size distributions, with no significant aggregation or precipitation observed (Fig. 1(i)). The average particle size of ND/P-CUR remained within the range of 118 to 124 nm, indicating excellent physical stability under refrigerated storage conditions.

In vitro drug release profiles (Fig. 1(j)) of free CUR, NS-CUR, ND-CUR, and ND/P-CUR were investigated using the dialysis method. Free CUR exhibited rapid release, with more than 86% of the drug diffusing into the release medium within the first 12 h. In contrast, NS-CUR, ND-CUR, and ND/P-CUR demonstrated sustained release profiles. Only approximately 60% of total CUR was released within 12 h, followed by gradual release over the subsequent 60 h. Compared with spherical nanostructures, disk-shaped NDs displayed a slightly slower release rate in the release medium. After 72 h, the cumulative release reached 91.8% for NS-CUR and 87.2% for ND-CUR, respectively. The difference may be attributed to the relatively larger specific surface area of NS-CUR, which facilitated faster drug diffusion. Notably, ND/P-CUR exhibited a release profile comparable to that of ND-CUR, with no obvious difference in release rate throughout the entire study period, indicating that peptide modification did not exert a significant influence on the drug release behavior of the NDs.

3.3 Cellular uptake

DiD was employed as a fluorescent probe to assess the cellular internalization of different formulations in CAFs using CLSM and flow cytometry. As shown in Fig. 2(b), both ND-DiD and ND/P-DiD demonstrated significantly higher intracellular fluorescence intensity compared to spherical nanostructures (NS-DiD), indicating a shape-dependent enhancement in cellular uptake for disk-shaped ND-DiD. Notably, ND/P-DiD exhibited the strongest fluorescence signal, suggesting that cCLT1 peptide modification further promoted internalization, presumably through receptor-mediated endocytosis. To confirm the involvement of cCLT1, a competitive blocking study was conducted. Preincubation with free cCLT1 peptide solution substantially reduced the intracellular fluorescence intensity of ND/P-DiD, clarifying that the enhanced uptake predominantly relied on the specific binding between cCLT1 and cFN (Fig. 2(a)).

For quantitative analysis, flow cytometry was employed to measure the fluorescence intensity of DiD in CAFs (Figs. 2(c) and 2(d)). Consistent with the CLSM observations, cells treated with ND/P-DiD exhibited the highest mean fluorescence intensity, which was approximately 4.54- and 2.73-fold higher than that of NS-DiD and ND-DiD, respectively. Collectively, these results substantiate the synergistic contribution of disk-shaped geometry and cCLT1-mediated cFN recognition, establishing a CAF-targeted nanoplatform with markedly improved cellular internalization (Fig. 2(a)).

To further confirm the selectivity of this targeting behavior, we conducted comparative cellular uptake assays using 4T1 breast cancer cells and quiescent NIH-3T3 fibroblasts. As shown in Fig. S3 in the ESM, ND-DiD was internalized more efficiently than NS-DiD in both 4T1 and NIH-3T3 cells, which might be attributed to the shape advantages of nanodisks. However, compared with unmodified ND-DiD, cCLT1 modification did not significantly enhance the uptake of ND/P-DiD in either cell type. Moreover, pretreatment with free cCLT1 peptide did not induce an obvious decrease in ND/P-DiD uptake. Notably, under comparable experimental conditions, both cell types showed significantly lower ND/P-DiD fluorescence intensity than CAFs. These findings indicated that cCLT1-mediated uptake enhancement was preferentially observed in CAFs, thereby supporting the selective CAF-targeting behavior of ND/P-CUR.

3.4 *In vitro* validation of cFN recognition by ND/P-CUR

We first performed a plasma stability assay to evaluate whether soluble plasma components, including pFN, affected the colloidal stability of ND/P-CUR in plasma. The results showed that no obvious increase in particle size was observed within 24 h, indicating that ND/P-CUR maintained good colloidal stability in the plasma (Fig. S4 in the ESM). These results suggested that soluble plasma components, including pFN, did not induce appreciable aggregation, bridging, or destabilization of ND/P-CUR under the tested conditions. Therefore, circulating pFN was

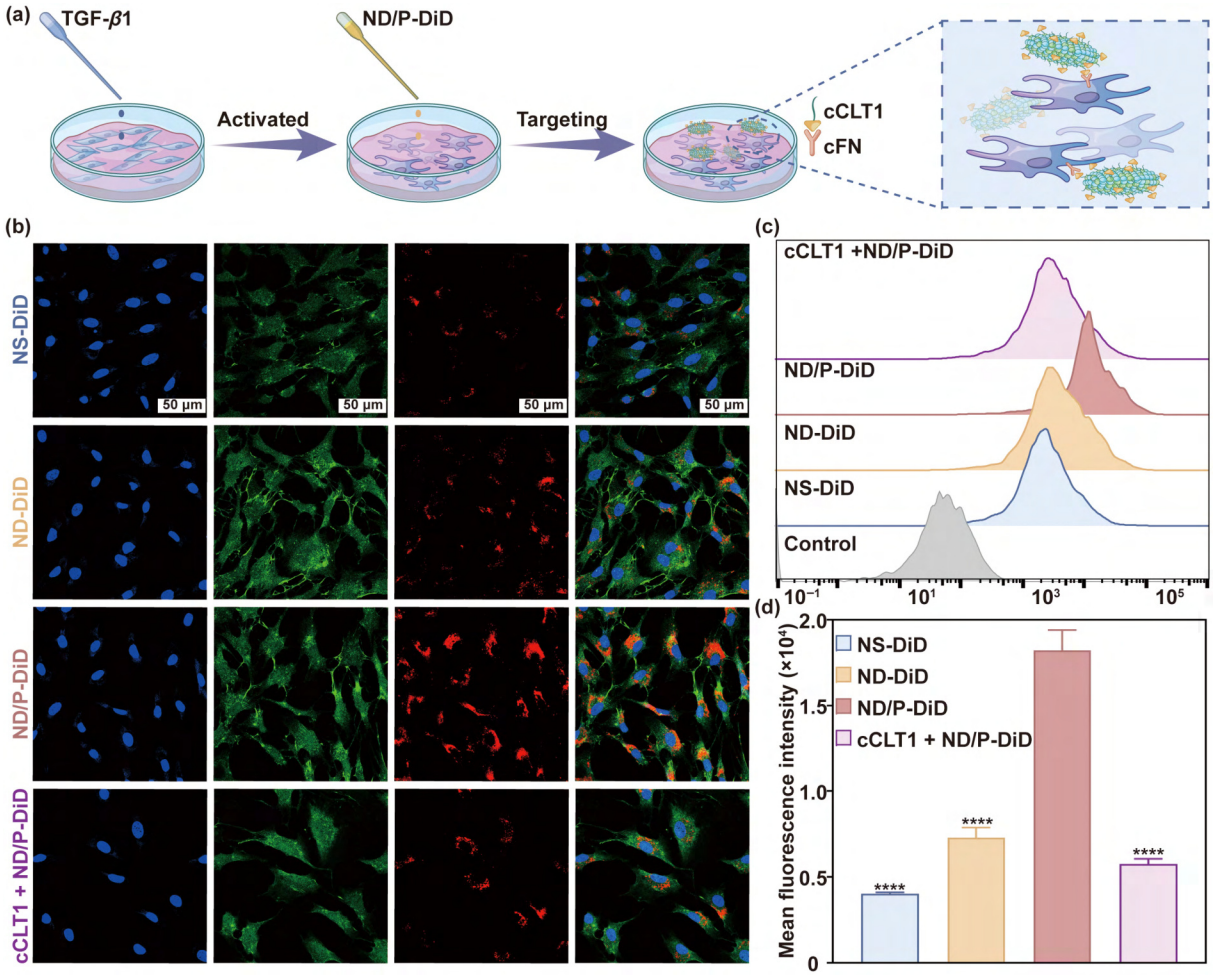

Figure 2 ND/P-CUR exhibited enhanced CAF-targeting capability *in vitro*. (a) Schematic illustration of the cellular uptake study in CAFs. (b) Representative CLSM images showing the cellular internalization profiles of NS-DiD, ND-DiD, ND/P-DiD, or cCLT1 + ND/P-DiD (cells pretreated with free cCLT1 peptide). (c) Flow cytometric analysis of cellular uptake profiles in CAFs following incubation with NS-DiD, ND-DiD, ND/P-DiD, or cCLT1 + ND/P-DiD (cells pretreated with free cCLT1 peptide). (d) Quantification of mean fluorescence intensity in CAFs from panel (c). Data are presented as mean ± SD ($n = 3$). ****$P < 0.0001$ vs. ND/P-DiD group.

unlikely to compromise the systemic stability of ND/P-CUR before tumor accumulation.

To further verify the specific recognition of cFN by cCLT1-functionalized NDs, a competitive uptake assay was also conducted using ND/P-DiD. As shown in Fig. S5 in the ESM, pFN preincubation caused no obvious reduction in the uptake of ND/P-DiD by CAFs compared with untreated (PBS-preincubated) or BSA-preincubated ND/P-DiD. In contrast, preincubation with cFN markedly inhibited ND/P-DiD internalization, reducing the relative uptake to 54.08% of that in the untreated group. These results suggested that pFN exerted limited interference with the CAF-targeting behavior of ND/P-DiD, while cFN competitively blocked ND/P-DiD uptake, further supporting the preferential recognition of cFN by cCLT1-functionalized NDs.

3.5 *In vitro* cytotoxicity

Based on the markedly enhanced cellular uptake of ND/P-CUR, its antiproliferative activity was further investigated in TGF-β1-activated NIH-3T3 cells (CAFs). As illustrated in Fig. 3(d), ND/P-CUR exhibited the strongest inhibitory effect on cell proliferation, followed by ND-CUR, NS-CUR, and free CUR. Specifically, ND-CUR decreased cell viability to 61.3%, which was lower than that observed for NS-CUR (70.6%), indicating that disk-shaped NDs conferred improved cytotoxicity relative to spherical NSs. Notably, ND/P-CUR treatment achieved the greatest suppression, further reducing cell viability to 50.3%. The enhanced antiproliferative efficacy of ND/P-CUR was consistent with the uptake results, supporting that cCLT1 decoration facilitated cellular internalization of CUR into activated CAFs, thereby amplifying its cytotoxic response.

To further evaluate the safety profile of different formulations, parallel experiments were conducted in quiescent NIH-3T3 cells under identical treatment conditions but in the absence of TGF-β1 stimulation. As shown in Fig. 3(e), all CUR formulations exhibited minimal cytotoxicity toward quiescent NIH-3T3 cells at the tested concentrations, with cell viability remaining above 95% in the ND/P-CUR group, comparable to that of the control group.

3.6 Suppression of CAF activation

Previous studies have shown that depletion of CAFs alone may promote cancer stemness and thus exacerbate metastatic progression [50]. Therefore, strategies aimed at reshaping CAFs into a quiescent state are increasingly considered advantageous. In this study, the expression level of α-SMA was detected to evaluate the efficacy of different formulations in suppressing CAF activation. Immunofluorescence analysis (Figs. 3(a) and 3(b)) revealed that

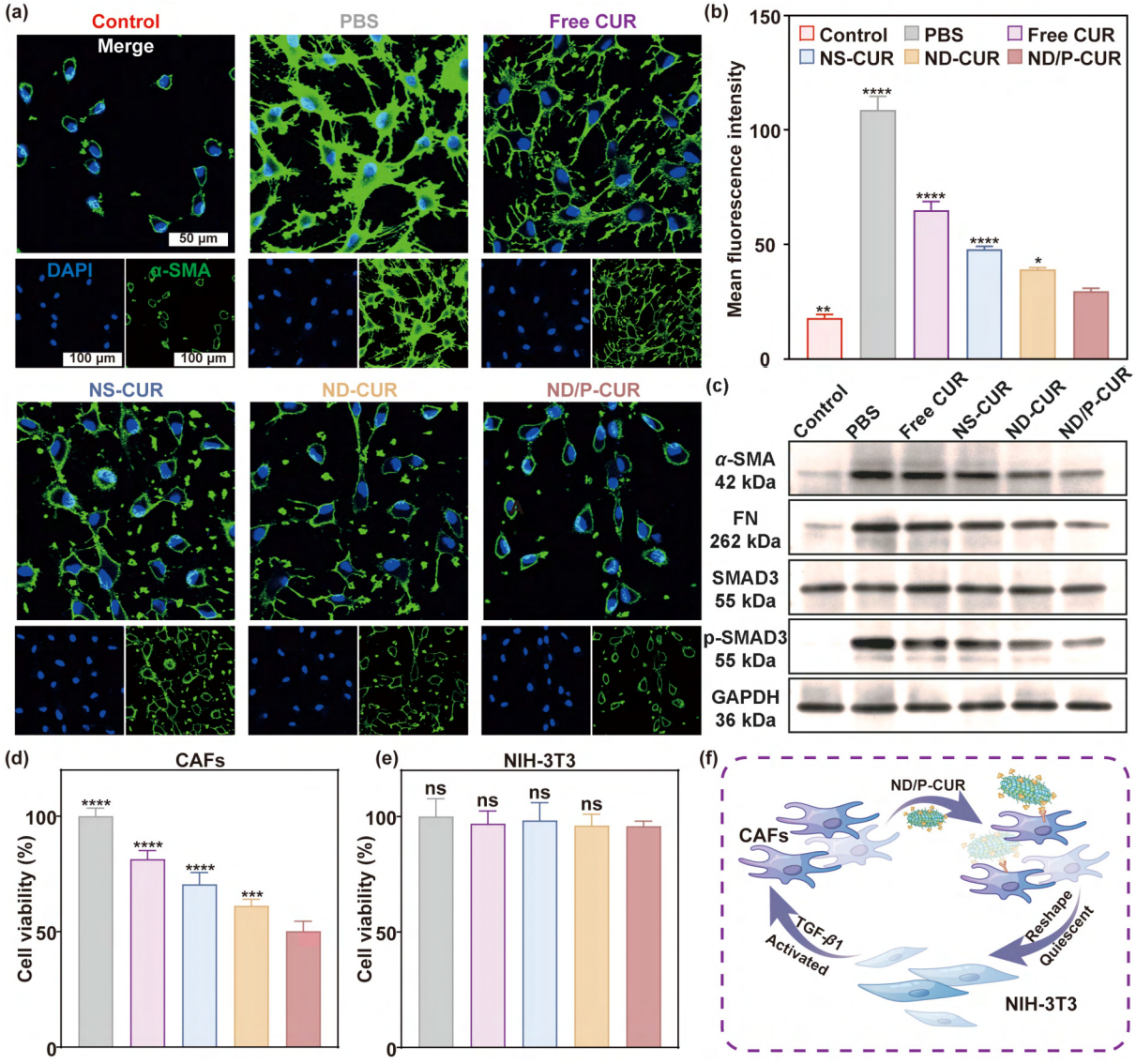

Figure 3 ND/P-CUR reprogrammed activated CAFs toward a quiescent phenotype. (a) Representative CLSM images of α-SMA immunofluorescence in NIH-3T3 fibroblasts (control) and CAFs (TGF-β1-activated NIH-3T3 cells) incubated with PBS, free CUR, NS-CUR, ND-CUR, or ND/P-CUR. (b) Semi-quantitative analysis of α-SMA fluorescence intensity from panel (a). Data are presented as mean ± SD (n = 3). *P < 0.05 vs. ND/P-CUR group; **P < 0.01 vs. ND/P-CUR group; ****P < 0.0001 vs. ND/P-CUR group. (c) Representative Western blot images of α-SMA, FN, SMAD3, and phosphorylated SMAD3 (p-SMAD3) in NIH-3T3 fibroblasts (control) and CAFs (TGF-β1-activated NIH-3T3 cells) incubated with PBS, free CUR, NS-CUR, ND-CUR, or ND/P-CUR. Cell viability of (d) CAFs (TGF-β1-activated NIH-3T3 cells) and (e) NIH-3T3 fibroblasts after incubation with PBS, free CUR, NS-CUR, ND-CUR, or ND/P-CUR. Data are presented as mean ± SD (n = 6). ***P < 0.001 vs. ND/P-CUR group; ****P < 0.0001 vs. ND/P-CUR group; ns, not significant, P > 0.05 vs. ND/P-CUR group. (f) Schematic illustration depicting the transition between activated CAFs and quiescent NIH-3T3 cells.

TGF-β1 stimulation markedly enhanced intracellular α-SMA expression, confirming the successful activation of NIH-3T3 cells toward CAFs phenotype. Treatment with free CUR resulted in a modest reduction in α-SMA fluorescence intensity, whereas both NS-CUR and ND-CUR induced a more pronounced attenuation. Notably, ND/P-CUR exhibited the weakest α-SMA signal among all groups, indicating the most effective suppression of CAF activation.

Western blot analysis (Fig. 3(c)) further corroborated the immunofluorescence findings. The α-SMA protein level was markedly reduced following treatment with CUR-based formulations, with ND/P-CUR achieving the greatest inhibitory effect. These findings demonstrated that ND/P-CUR effectively suppressed α-SMA expression and mitigated CAF activation.

Since activated CAFs are major contributors to ECM overproduction, we further examined the expression of FN, a key ECM protein produced by CAFs. As shown in Fig. 3(c), TGF-β1 stimulation markedly increased FN expression in CAFs, whereas ND/P-CUR treatment resulted in the most pronounced reduction in FN expression among all CUR-based formulations. These results indicated that ND/P-CUR not only suppressed CAF activation but also reduced FN expression in activated CAFs, suggesting its potential to attenuate excessive ECM deposition and contribute to TME remodeling.

We also investigated the CAF activation-related TGF-β/SMAD3 signaling pathway, which plays a key role in fibroblast activation [51]. Western blot analysis (Fig. 3(c)) showed that activated CAFs exhibited a substantial increase in the phosphorylation level of

SMAD3 (p-SMAD3) compared with quiescent NIH-3T3 fibroblasts. ND-CUR downregulated the p-SMAD3 level more effectively than NS-CUR, suggesting the shape advantages of nanodisks. More importantly, cells treated with ND/P-CUR showed the lowest p-SMAD3 level among all groups, indicating that cCLT1-mediated CAF targeting enhanced the ability of CUR to suppress SMAD3 phosphorylation within the TGF-β/SMAD3 signaling pathway.

Taken together, ND/P-CUR efficiently reprogrammed CAFs toward a less activated state, as evidenced by decreased α-SMA expression, reduced FN level, and suppressed SMAD3 phosphorylation. This CAF-reprogramming effect consequently contributed to TME remodeling and the enhanced therapeutic efficacy observed in this study (Fig. 3(f)).

3.7 *In vitro* cell migration assay

Suppression of CAF activation can disrupt the crosstalk between CAFs and tumor cells, thereby limiting metastatic progression [52]. In this study, the migration behavior of 4T1 cells was evaluated using CM collected from differently treated CAFs in a wound healing assay (Fig. 4(a)). As shown in Fig. 4(b), a substantial reduction in the wound area was observed in the control group after 24 h, indicating that the CM derived from activated CAFs strongly promoted 4T1 cell migration. By comparison, when CAFs were treated with CUR-based formulations, the corresponding CM's function on promoting migration was attenuated to varying extents. Quantitative analysis (Fig. 4(c)) revealed that the wound healing rates in NS-CUR and ND-CUR groups were 44.7% and 35.0%, respectively. Among all groups, ND/P-CUR demonstrated the strongest inhibition of migration with a wound healing rate of 27.0%, whereas free CUR showed the weakest suppression effect, as reflected by a wound healing rate of 52.0%. The superior anti-migratory effect observed in the ND/P-CUR group was consistent with its enhanced intracellular delivery and stronger suppression of CAF activation.

3.8 Tumor spheroid formation and imaging

The penetration behavior of different formulations was evaluated in MCTs constructed from 4T1 cells and CAFs. After 6 days of culture, the spheroids formed compact three-dimensional structures with an average diameter of approximately 400 μm (Fig. 5(a)). In the NS-DiD group, fluorescence signals were predominantly localized at the periphery of the spheroids, indicating limited diffusion into the dense matrix. By comparison, ND-DiD moderately improved penetration into MCTs, as fluorescence signals extended beyond the outer layers, although the distribution remained largely confined to the peripheral regions. In contrast, ND/P-DiD achieved markedly enhanced penetration, with strong fluorescence signals detected across the spheroid cross-section, including the central core. Fluorescence intensity profiles (Fig. 5(b)) further confirmed the greater penetration depth of ND/P-DiD compared with NS-DiD and ND-DiD, demonstrating the superior penetration capability of cCLT1-decorated NDs in MCTs.

3.9 Biodistribution study

Next, the biodistribution study was conducted in BALB/c mice bearing orthotopic breast tumors established by co-implantation of 4T1 and NIH-3T3 cells. *Ex vivo* fluorescence imaging was performed at 2, 4, 8, and 24 h after intravenous administration of free DiD, NS-DiD, ND-DiD, or ND/P-DiD. Representative fluorescence images of excised tumors and major organs are shown in Fig. 6(a). Clear formulation- and time-dependent distribution patterns were observed among different groups.

At 2 h post-injection, obvious fluorescence signals were observed primarily in the liver, which was consistent with the immediate sequestration of nanoparticles by the reticuloendothelial system. During this period, free DiD exhibited minimal fluorescence accumulation at the tumor site, whereas NS-DiD showed detectable but relatively weak tumor signals. In comparison, ND-DiD achieved visibly higher tumor accumulation, highlighting a shape-dependent improvement in tumor localization. Importantly, ND/P-

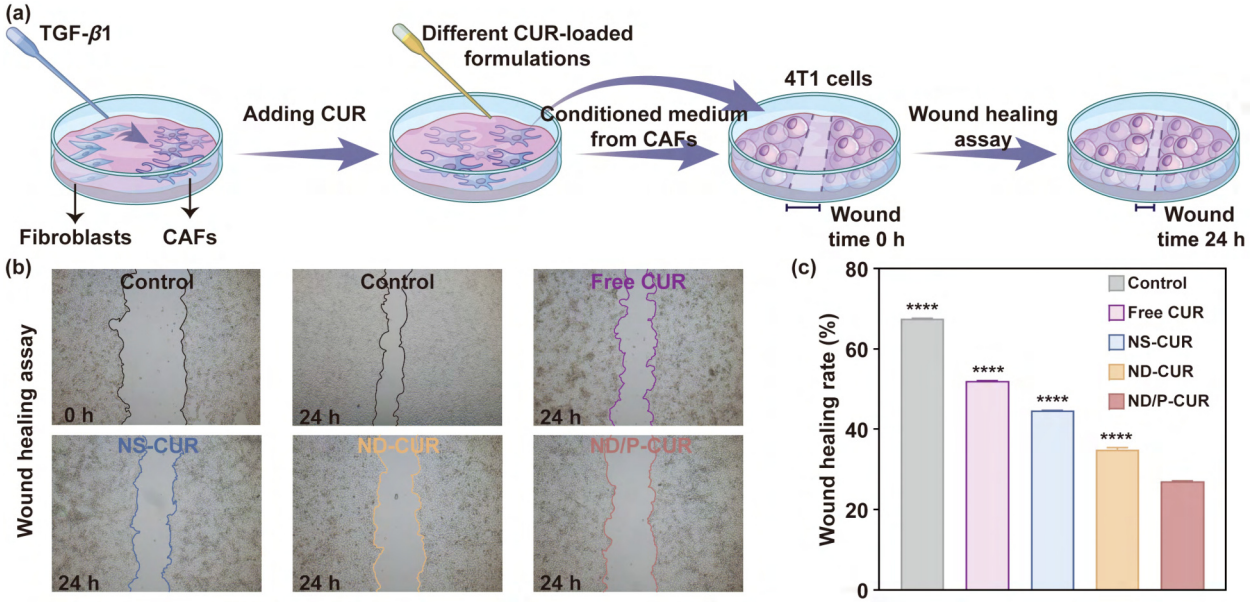

Figure 4 ND/P-CUR attenuated CAF-mediated tumor cell migration. (a) Schematic illustration of the experimental design for the wound healing assay using CM collected from CAFs receiving different treatments. (b) Representative images of scratch wounds in 4T1 cell monolayers at 0 and 24 h after incubation with CM collected from CAFs treated with PBS, free CUR, NS-CUR, ND-CUR, or ND/P-CUR. (c) Quantification of wound healing rates based on the wound area measured by ImageJ at 0 and 24 h. Data are presented as mean ± SD ($n = 3$). ****$P < 0.0001$ vs. ND/P-CUR group.

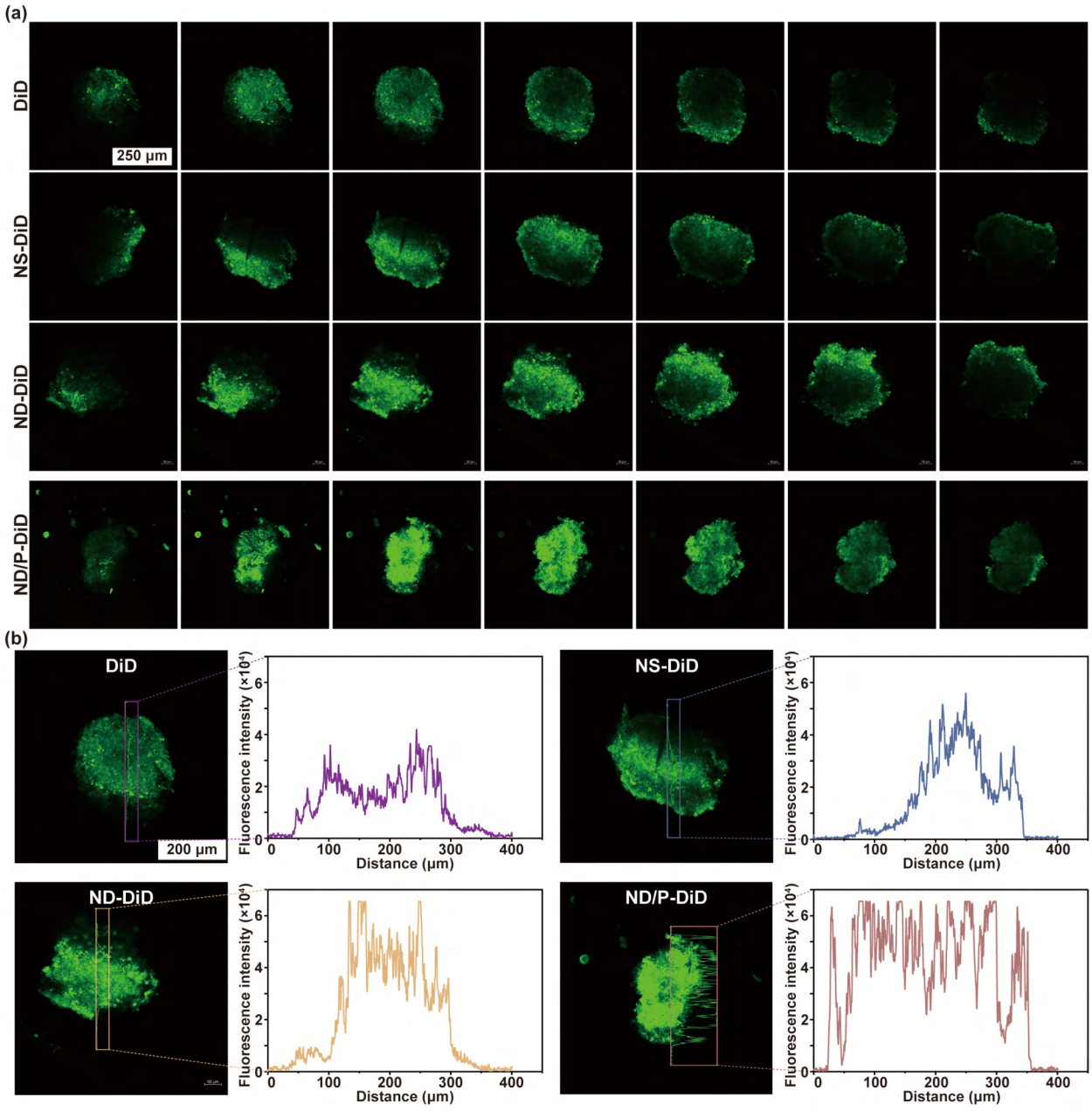

Figure 5 ND/P-CUR enhanced penetration into MCTs. (a) Representative Z-stack confocal images showing the fluorescence distribution of DiD, NS-DiD, ND-DiD, or ND/P-DiD within the MCTs. (b) Corresponding fluorescence intensity profiles across the spheroid cross-section, with signals quantified within the central 400 μm region to evaluate penetration depth.

DiD displayed the strongest fluorescence intensity within tumors. Tumor accumulation of ND/P-DiD increased over time and reached a maximum at 4 h post-injection. Semi-quantitative analysis (Fig. 6(b)) demonstrated that the tumor fluorescence intensity in the ND/P-DiD group was approximately 1.66-fold higher than that in the ND-DiD group and 2.38-fold higher than that in the NS-DiD group at 4 h. Although ND-DiD also showed enhanced tumor accumulation relative to NS-DiD and free DiD, its fluorescence signal remained lower than that of ND/P-DiD throughout the whole observation period, indicating an additional targeting contribution from cCLT1 decoration. To further evaluate organ-level distribution, fluorescence intensity was normalized and presented as stacked bar charts (Fig. 6(c)) and heatmaps (Fig. S6 in the ESM). These analyses further demonstrated that ND/P-DiD showed preferential tumor accumulation compared with other groups, which could be attributed to the shape advantages of NDs combined with cCLT1-mediated targeting of CAFs within stromal regions.

3.10 *In vivo* antitumor efficacy evaluation

The antitumor efficacy was also evaluated in BALB/c mice bearing orthotopic breast tumors. When the tumor volume reached approximately 103.7 mm^3 on day 9, mice were administered intravenously with the corresponding preparations every 2 days for a total of 4 times (Fig. 7(a)). Tumor volume was recorded throughout the study, and the tumor growth curves are presented in Fig. 7(c).

Tumors in the saline and free CUR groups increased rapidly

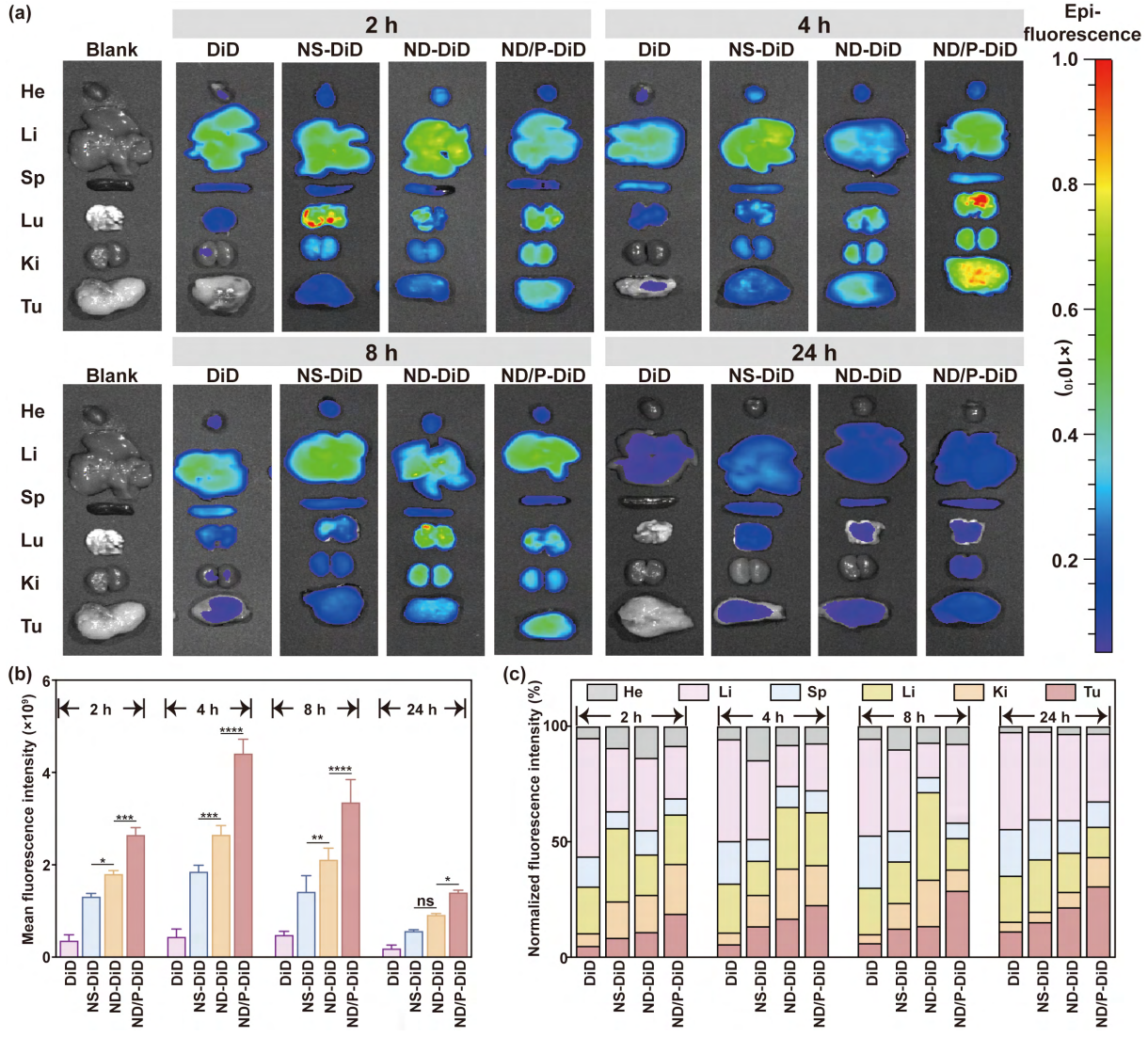

Figure 6 ND/P-DiD exhibited enhanced tumor localization in orthotopic breast tumor-bearing mice. (a) Representative *ex vivo* fluorescence images of major organs and tumors collected at 2, 4, 8, and 24 h after intravenous injection of free DiD, NS-DiD, ND-DiD, or ND/P-DiD. He, Li, Sp, Lu, Ki and Tu represent heart, liver, spleen, lung, kidney, and tumor, respectively. (b) Semi-quantitative analysis of fluorescence intensity in tumor tissues from panel (a). Data are presented as mean ± SD (n = 3). *P < 0.05; **P < 0.01; ***P < 0.001; ****P < 0.0001; ns, not significant, P > 0.05. (c) Stacked histogram of normalized fluorescence distribution in major organs and tumors at the indicated time points following injection of free DiD, NS-DiD, ND-DiD, or ND/P-DiD.

during the observation period, indicating aggressive tumor progression and the limited therapeutic efficacy of free CUR. Treatment with NS-CUR moderately suppressed tumor growth, whereas ND-CUR exhibited a more pronounced inhibitory effect, suggesting that the nanodisk structure contributed to enhanced therapeutic performance. Among all treatment groups, ND/P-CUR resulted in the most significant tumor growth suppression, as evidenced by the lowest tumor volume. On day 29, the average tumor volume in the saline group was approximately 2.95-fold higher than that of the ND/P-CUR group. The tumor inhibition rate (TIR) relative to the saline group was calculated (Figs. 7(d) and 7(e)). The TIR was 70.3% in the ND/P-CUR group, which was markedly higher than in the ND-CUR (51.4%), NS-CUR (42.7%), and free CUR (25.5%) groups, consistent with the tumor growth curves. Meanwhile, no significant body weight loss was observed in mice treated with ND/P-CUR (Fig. 7(f)), indicating favorable systemic tolerability of ND/P-CUR at the administered dose.

Histological analysis of tumor sections further supported the superior antitumor efficacy of ND/P-CUR. As shown by H&E staining (Fig. 7(g)), tumors from the saline group displayed dense cellular architecture and typical malignant features, whereas increased necrotic regions and reduced tumor cell density were observed in tumors treated with ND-CUR and ND/P-CUR. Notably, tumors from the ND/P-CUR group exhibited the most extensive structural disruption, characterized by enlarged necrotic areas and reduced cellular density, further supporting its strong antitumor potency.

3.11 *In vivo* antimetastatic efficacy evaluation

The antimetastatic efficacy of different CUR-loaded formulations was subsequently evaluated. Pulmonary metastatic burden was assessed by bioluminescence imaging (BLI) and histological analysis at the experimental endpoint (Fig. 8(a)). As shown in Fig. 8(b), strong bioluminescence signals were detected in the lungs of mice treated with saline, indicating extensive pulmonary metastasis. Free CUR treatment slightly reduced the lung-associated

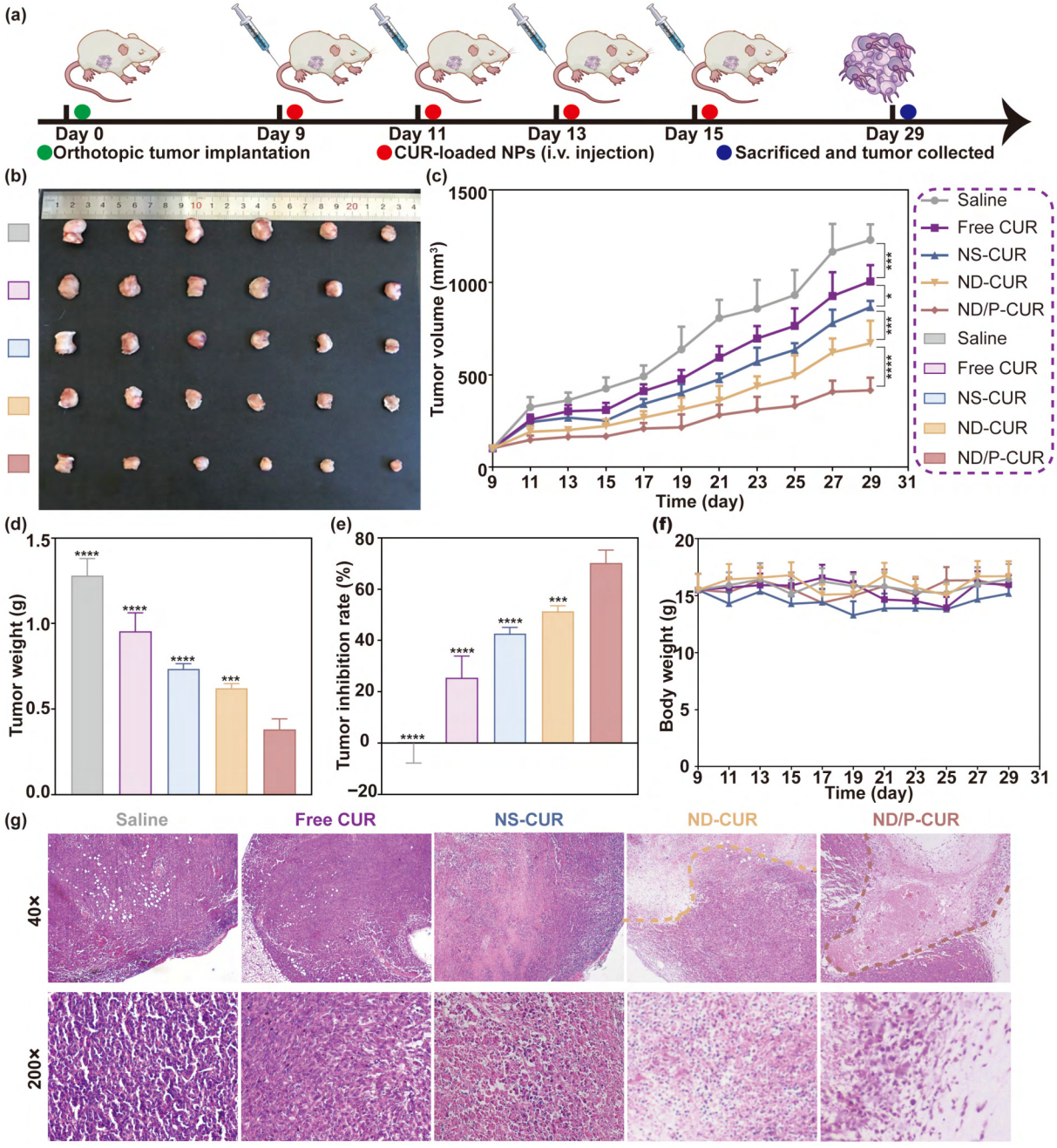

Figure 7 ND/P-CUR showed potent suppression of tumor growth in orthotopic breast tumor-bearing mice. (a) Schematic illustration of the treatment regimen in the antitumor study. (b) Representative photographs of excised tumors collected at the end of different treatments. (c) Tumor growth curves of different groups throughout the treatment period. Data are presented as mean ± SD (n = 6). *P < 0.05; ***P < 0.001; ****P < 0.0001. (d) Tumor weights and (e) corresponding tumor inhibition rates in different groups at the study endpoint. Data are presented as mean ± SD (n = 6). ***P < 0.001 vs. ND/P-CUR group; ****P < 0.0001 vs. ND/P-CUR group. (f) Body weight changes of mice throughout the treatment period. (g) Representative H&E staining images of excised tumor tissues after different treatments.

bioluminescence intensity. In comparison, mice treated with NS-CUR exhibited a moderate decrease in metastatic signals, whereas ND-CUR treatment further reduced lung bioluminescence. Notably, minimal lung metastatic bioluminescence signals were detected in the ND/P-CUR group, suggesting pronounced inhibition of lung metastasis. Semi-quantitative analysis of lung bioluminescence intensity (Fig. 8(c)) further confirmed these observations. The average total photon flux in the ND/P-CUR group was approximately 364-, 55-, 11-, and 5-fold lower than that in the saline, free CUR, NS-CUR, and ND-CUR groups, respectively.

Histological examination of lung sections by H&E staining (Fig. 8(d)) provided additional evidence of the antimetastatic effect. Numerous metastatic lesions were observed in the lungs from the saline and free CUR groups. In contrast, the NS-CUR and ND-CUR groups showed fewer metastatic foci, whereas the ND/P-CUR group exhibited the most pronounced reduction in pulmonary metastatic nodules, consistent with the BLI results.

3.12 Antitumor and antimetastatic mechanism study

To investigate the mechanisms underlying the antitumor and

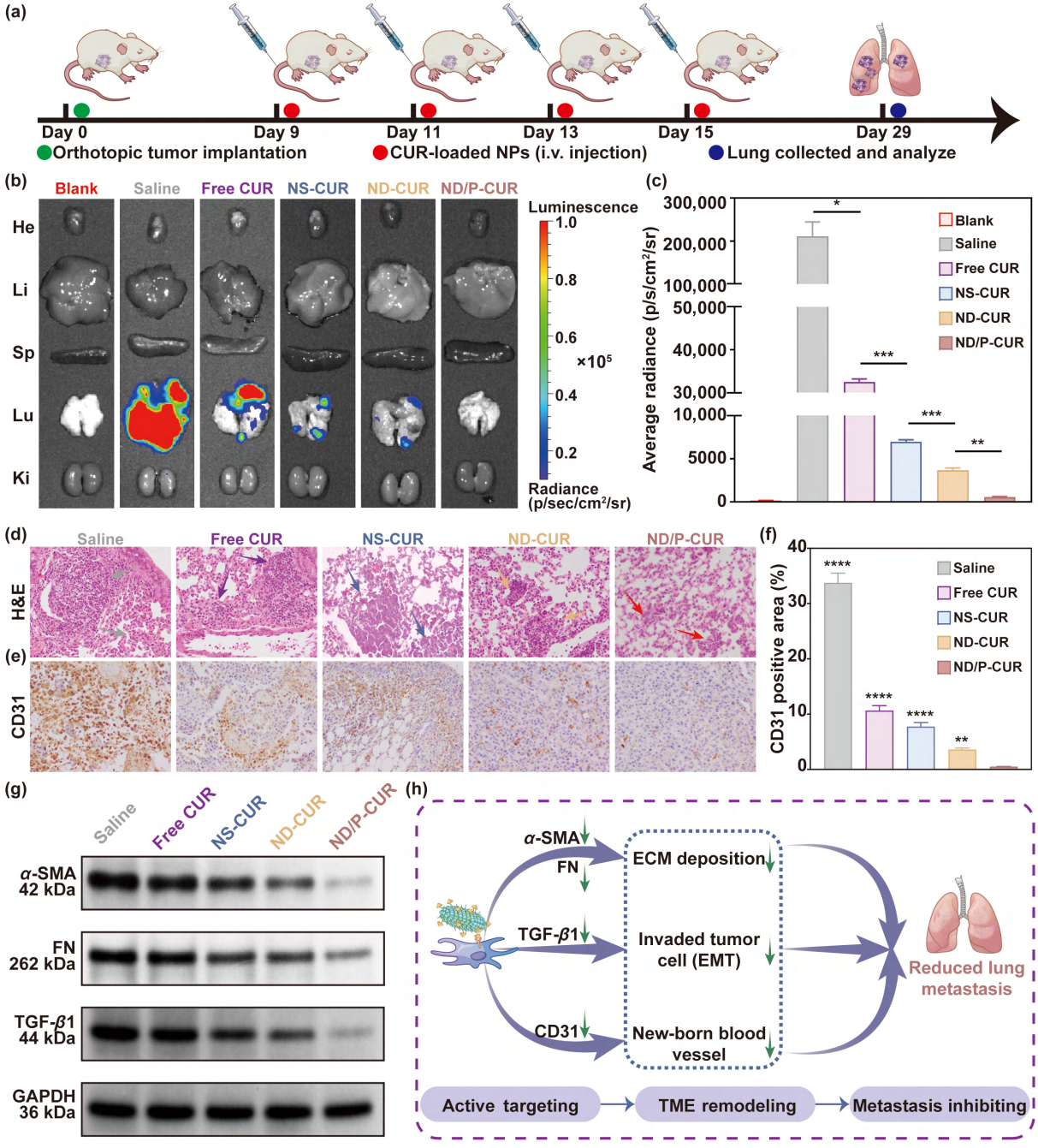

Figure 8 ND/P-CUR inhibited lung metastasis in orthotopic breast tumor-bearing mice by remodeling the TME. (a) Schematic illustration of the treatment strategy in the antimetastatic study. (b) Representative *ex vivo* bioluminescence images of excised lungs at the end of different treatments. (c) Semi-quantitative analysis of lung bioluminescence intensity from panel (b). Data are presented as mean ± SD (n = 3). *P < 0.05; **P < 0.01; ***P < 0.001. (d) Representative H&E staining images of lung sections after different treatments. (e) Representative CD31 immunohistochemical staining images of excised tumor tissues after different treatments. (f) Semi-quantitative analysis of CD31 staining results. Data are presented as mean ± SD (n = 3). **P < 0.01 vs. ND/P-CUR group; ****P < 0.0001 vs. ND/P-CUR group; ns, not significant, P > 0.05 vs. ND/P-CUR group. (g) Representative Western blot images of α-SMA, FN, and TGF-β1 in tumor tissues following different treatments. (h) Schematic illustration of the mechanisms underlying the antitumor and antimetastatic effects of ND/P-CUR.

antimetastatic effects of ND/P-CUR, several key pathological processes, including angiogenesis, ECM deposition, and TGF-β1 expression, were evaluated.

CD31 immunohistochemical staining was first performed to assess tumor angiogenesis (Fig. 8(e)). Semi-quantitative analysis demonstrated that tumors treated with ND/P-CUR displayed a significant reduction in CD31-positive microvessel density compared with the control and other CUR-treated groups (Fig. 8(f)). These findings suggested that ND/P-CUR effectively inhibited the formation of new-born blood vessels, thus limiting the supply of nutrients and oxygen required for tumor growth and metastatic dissemination [53–56].

Considering that excessive ECM deposition facilitated tumor cell invasion and metastasis [57], the expression levels of FN and α-SMA were subsequently examined by WB analysis (Fig. 8(g)). Among all treatment groups, ND/P-CUR exhibited the most

pronounced downregulation of FN expression. In parallel, α-SMA expression was also markedly suppressed in the ND/P-CUR group. These results highlighted the effectiveness of ND/P-CUR in attenuating CAF-associated ECM deposition in tumor tissues.

Given the pivotal role of TGF-β1-mediated tumor-stroma crosstalk in driving epithelial-mesenchymal transition (EMT) and metastatic progression, we further evaluated TGF-β1 expression in tumor tissues [58, 59]. As depicted in Fig. 8(g), ND/P-CUR treatment resulted in a marked decrease in TGF-β1 expression compared with the control and other treatment groups. Although EMT markers were not directly assessed in this study, the reduced TGF-β1 level indicated potential attenuation of EMT-related signaling pathways. Such modulation might impair the acquisition of mesenchymal traits by tumor cells, thereby limiting their migratory and invasive capacity, which ultimately contributed to the observed antimetastatic outcome.

Taken together, these findings suggested that the enhanced antitumor and antimetastatic efficacy of ND/P-CUR could be mediated through multiple coordinated mechanisms, including suppression of tumor angiogenesis, attenuation of ECM deposition, and downregulation of TGF-β1 expression (Fig. 8(h)).

4 Discussion

Breast cancer remains one of the leading causes of cancer-related mortality among women, with metastasis being the principal driver of treatment failure and poor prognosis. Accordingly, novel therapeutic strategies are urgently needed to improve tumor targeting and suppress metastatic progression. In the present study, we developed cCLT1-decorated nanodisks (ND/P-CUR) as a CAF-targeted nanoplatform for CUR delivery. Our results demonstrated that ND/P-CUR achieved enhanced tumor accumulation through cCLT1-mediated recognition of cFN in CAF-enriched stroma. The superior targeting capability was accompanied by effective CAF reprogramming and TME remodeling, collectively translating into improved suppression of primary tumor growth and metastatic progression.

The physicochemical properties of nanoparticles are known to influence their biological behaviors, among which particle shape plays an important role. In this study, disk-shaped NDs were selected as the delivery carrier, and their characteristics were systematically compared with conventional nanospheres (NSs) both *in vitro* and *in vivo*. Stability assessments showed that both NDs and NSs maintained favorable physical stability at 4 °C. Moreover, *in vitro* release studies revealed a slower and more sustained release profile of CUR from NDs relative to NSs, which may contribute to reduced premature drug leakage and prolonged drug retention. Cellular uptake and tumor spheroid penetration experiments further indicated that NDs were internalized more efficiently and penetrated more deeply into dense multicellular tumor spheroids. Consistently, *in vivo* biodistribution studies confirmed the superior passive targeting capability of NDs compared with NSs, which correlated well with the enhanced antitumor and antimetastatic efficacy observed in the therapeutic studies.

The superior performance of NDs over NSs can be attributed to several advantages associated with their disk-like geometry. First, the higher aspect ratio of NDs provides a larger contact interface with the cell membrane than NSs, thereby facilitating more extensive ligand-receptor interactions and promoting cellular internalization. Second, NDs integrate the geometric benefits of both spherical NSs and elongated nanorods. Owing to their anisotropic structure, NDs can preferentially orient themselves perpendicular to endothelial gaps, enabling more efficient penetration through the inter-endothelial junctions of tumor vessels [60]. Third, NDs exhibit a stronger margination tendency toward vascular walls, which may further enhance adhesion to tumor endothelium and facilitate extravasation into tumors [61, 62]. Collectively, these geometric features endow disk-shaped NDs with distinct advantages in cellular uptake, tumor accumulation, and therapeutic efficacy, which are challenging to achieve simultaneously with conventional spherical nanocarriers.

A great deal of evidence indicates that TME provides a permissive "soil" for tumor progression, in which CAFs are the major stromal components and crosstalk centers [63]. CAFs promote tumor growth and metastasis by secreting various chemokines, cytokines, and ECM components. Therefore, targeting CAFs represents a promising therapeutic strategy for remodeling TME and inhibiting metastasis.

In this study, ND/P-CUR was designed to modulate CAFs through cCLT1-mediated FN recognition. Notably, FN exists in two major forms based on its solubility, including soluble disulfide-bonded dimeric pFN and insoluble cFN present on the cell surface or within the ECM. Our results suggested that ND/P-CUR could distinguish these two types of FN and preferentially interact with cFN rather than soluble pFN. This difference may be attributed to the distinct molecular conformation and spatial accessibility of these two FN forms [64]. Compared with the compact conformation of pFN [65], cell- or matrix-assembled cFN in the tumor stroma may expose distinct ligand-accessible binding sites during fibrillar organization, thereby favoring cCLT1-mediated recognition [66, 67]. Such specific recognition of cFN can enhance the local accumulation of ND/P-CUR in the tumor stroma and facilitate its subsequent internalization by CAFs, thereby providing a basis for its CAF-targeted therapeutic effects.

This CAF-targeting behavior may facilitate CAF reprogramming and TME remodeling, as reflected by suppressed angiogenesis, attenuated ECM deposition, and decreased TGF-β1 expression, consequently contributing to the antitumor and antimetastatic efficacy of ND/P-CUR. First, immunohistochemical analysis revealed a significant reduction in CD31-positive microvessel density following ND/P-CUR treatment, suggesting effective inhibition of tumor angiogenesis. As pathological neovascularization supports tumor growth and provides routes for hematogenous metastasis, angiogenesis suppression may constitute a critical mechanism underlying the therapeutic efficacy of ND/P-CUR. In parallel, treatment with ND/P-CUR markedly reduced FN and α-SMA expression in tumor tissues, suggesting effective suppression of CAF activation and ECM deposition. Given the critical role of ECM in facilitating tumor invasion and metastasis, attenuation of ECM deposition could contribute to the inhibition of metastatic progression. Furthermore, ND/P-CUR markedly decreased intratumoral TGF-β1 levels, indicating disruption of CAF-associated cytokine signaling involved in maintaining tumor-stroma crosstalk. As TGF-β1 is also implicated in tumor cell proliferation and epithelial-mesenchymal transition, its downregulation may provide another mechanistic basis for the restrained primary tumor growth and metastatic dissemination observed *in vivo*.

Future research can explore the combination strategies integrating CAF regulation with chemotherapy, immunotherapy, or other targeted therapies. Such approaches may further amplify

therapeutic efficacy by concurrently normalizing the TME and sensitizing tumor cells to therapeutic interventions. Nevertheless, the molecular pathways through which ND/P-CUR induces CAF reprogramming remain to be fully elucidated, and the long-term biosafety of ND/P-CUR requires additional evaluation.

5 Conclusions

In summary, this study developed a CAF-targeted nanotherapeutic strategy for breast cancer based on cCLT1-functionalized nanodisks (ND/P-CUR). By integrating the shape-dependent delivery advantages of nanodisks with cCLT1-mediated cFN recognition, ND/P-CUR achieved enhanced cellular internalization, improved tumor penetration, and greater intratumoral accumulation. Rather than eliminating CAFs directly, this strategy effectively induced CAF reprogramming, thereby reshaping the tumor stroma and alleviating the prometastatic microenvironment. Such stromal remodeling was accompanied by impaired tumor angiogenesis, reduced ECM deposition, and attenuated TGF-β1 expression, which collectively contributed to the superior antitumor and antimetastatic efficacy of ND/P-CUR. Overall, these findings highlight the therapeutic potential of combining nanocarrier shape engineering with CAF targeting and suggest that this strategy could be developed into a promising therapeutic platform for other types of cancers with similar CAF-rich microenvironments.

Electronic Supplementary Material: Supplementary material (chemical and structural verification of DSPE-PEG2000-cCLT1, cellular uptake and competitive uptake assays, plasma stability and physicochemical characterization of CUR-loaded nanosystems, and detailed antibody information used in the study) is available in the online version of this article at https://doi.org/10.26599/NR.2026.94908905.

Data availability

All data needed to support the conclusions in the paper are presented in the manuscript and/or the Electronic Supplementary Material. Additional data related to this paper may be requested from the corresponding author upon request.

Acknowledgements

This work was supported by the National Natural Science Foundation of China (No. 82504669), Beijing Research Ward Excellence Program, BRWEP(No. BRWEP2024W102090109), Beijing Natural Science Foundation-Haidian Original Innovation Joint Fund (No. L232015), and Beijing Natural Science Foundation (No. 7264274).

Declaration of competing interest

All the contributing authors report no conflict of interests in this work.

Author contribution statement

C. C. Z.: Conceptualization, funding acquisition, writing – original draft, methodology, data curation, software, investigation. S. S. X.: Writing – review & editing, methodology, investigation, software. M. Z. C.: Methodology, data curation, formal analysis. X. X. Y: Validation, data curation. J. W.: Writing – review & editing, supervision. Q. C.: Writing – review & editing. P. G.: Supervision, resources, funding acquisition, conceptualization. All the authors have approved the final manuscript.

Informed consent

Not applicable.

Ethics statement

The animal experiments were carried out following the institutional guidelines and approved by the Animal Ethics Committee of the Animal Ethics Committee of the Institute of Materia Medica, Chinese Academy of Medical Sciences and Peking Union Medical College (approval number: 00008419).

Use of AI statement

None.

References

[1] Bray, F.; Laversanne, M.; Sung, H.; Ferlay, J.; Siegel, R. L.; Soerjomataram, I.; Jemal, A. Global cancer statistics 2022: GLOBOCAN estimates of incidence and mortality worldwide for 36 cancers in 185 countries. *CA Cancer J. Clin.* **2024**, *74*, 229–263.

[2] Schmid, P.; Cortes, J.; Dent, R.; McArthur, H.; Pusztai, L.; Kümmel, S.; Denkert, C.; Park, Y. H.; Hui, R. N.; Harbeck, N. et al. Overall survival with pembrolizumab in early-stage triple-negative breast cancer. *N. Engl. J. Med.* **2024**, *391*, 1981–1991.

[3] Jiang, Z. F.; Ouyang, Q. C.; Sun, T.; Zhang, Q. Y.; Teng, Y. E.; Cui, J. W.; Wang, H. B.; Yin, Y. M.; Wang, X. J.; Zhou, X. et al. Toripalimab plus nab-paclitaxel in metastatic or recurrent triple-negative breast cancer: A randomized phase 3 trial. *Nat. Med.* **2024**, *30*, 249–256.

[4] Weigelt, B.; Peterse, J. L.; van't Veer, L. J. Breast cancer metastasis: Markers and models. *Nat. Rev. Cancer* **2005**, *5*, 591–602.

[5] DeSantis, C.; Ma, J.; Bryan, L.; Jemal, A. Breast cancer statistics, 2013. *CA Cancer J. Clin.* **2014**, *64*, 52–62.

[6] Nardin, S.; Mora, E.; Varughese, F. B.; D'Avanzo, F.; Vachanaram, A. R.; Rossi, V.; Saggia, C.; Rubinelli, S.; Gennari, A. Breast cancer survivorship, quality of life, and late toxicities. *Front. Oncol.* **2020**, *10*, 864.

[7] Liang, Y. R.; Zhang, H. W.; Song, X. J.; Yang, Q. F. Metastatic heterogeneity of breast cancer: Molecular mechanism and potential therapeutic targets. *Semin. Cancer Biol.* **2020**, *60*, 14–27.

[8] Guo, R. Z.; Zhang, Z. Z.; Zhang, S. Y.; Gai, T. T.; Yu, H. Z.; Su, L.; Yin, H.; Wang, X. H.; Zhang, Y. F. Innovative nanocarriers: Synthetic and biomimetic strategies for enhanced drug delivery. *Mater. Today Bio* **2025**, *34*, 102180.

[9] Mitchell, M. J.; Billingsley, M. M.; Haley, R. M.; Wechsler, M. E.; Peppas, N. A.; Langer, R. Engineering precision nanoparticles for drug delivery. *Nat. Rev. Drug Discovery* **2021**, *20*, 101–124.

[10] Kinnear, C.; Moore, T. L.; Rodriguez-Lorenzo, L.; Rothen-Rutishauser, B.; Petri-Fink, A. Form follows function: Nanoparticle shape and its implications for nanomedicine. *Chem. Rev.* **2017**, *117*, 11476–11521.

[11] Bariwal, J.; Ma, H. R.; Altenberg, G. A.; Liang, H. J. Nanodiscs: A versatile nanocarrier platform for cancer diagnosis and treatment. *Chem. Soc. Rev.* **2022**, *51*, 1702–1728.

[12] Huang, Y.; Wang, J.; Jiang, K. R.; Chung, E. J. Improving kidney targeting: The influence of nanoparticle physicochemical properties on kidney interactions. *J. Control. Release* **2021**, *334*, 127–137.

[13] Li, S. L.; Nickels, J.; Palmer, A. F. Liposome-encapsulated actin-

hemoglobin (LEAcHb) artificial blood substitutes. *Biomaterials* **2005**, *26*, 3759–3769.
[14] Calderon, A. J.; Bhowmick, T.; Leferovich, J.; Burman, B.; Pichette, B.; Muzykantov, V.; Eckmann, D. M.; Muro, S. Optimizing endothelial targeting by modulating the antibody density and particle concentration of anti-ICAM coated carriers. *J. Control. Release* **2011**, *150*, 37–44.
[15] Acharya, B.; Behera, A.; Behera, S.; Moharana, S. Recent advances in nanotechnology-based drug delivery systems for the diagnosis and treatment of reproductive disorders. *ACS Appl. Bio Mater.* **2024**, *7*, 1336–1361.
[16] Kuai, R.; Ochyl, L. J.; Bahjat, K. S.; Schwendeman, A.; Moon, J. J. Designer vaccine nanodiscs for personalized cancer immunotherapy. *Nat. Mater.* **2017**, *16*, 489–496.
[17] Gajski, G.; Garaj-Vrhovac, V. Melittin: A lytic peptide with anticancer properties. *Environ. Toxicol. Pharmacol.* **2013**, *36*, 697–705.
[18] Gao, J.; Xie, C.; Zhang, M. F.; Wei, X. L.; Yan, Z. Q.; Ren, Y. C.; Ying, M.; Lu, W. Y. RGD-modified lipid disks as drug carriers for tumor targeted drug delivery. *Nanoscale* **2016**, *8*, 7209–7216.
[19] Palange, A. L.; Palomba, R.; Rizzuti, I. F.; Ferreira, M.; Decuzzi, P. Deformable discoidal polymeric nanoconstructs for the precise delivery of therapeutic and imaging agents. *Mol. Ther.* **2017**, *25*, 1514–1521.
[20] Kwa, M. Q.; Herum, K. M.; Brakebusch, C. Cancer-associated fibroblasts: How do they contribute to metastasis. *Clin. Exp. Metastasis* **2019**, *36*, 71–86.
[21] Xu, S. L.; Wang, T.; Hu, X. C.; Deng, H.; Zhang, Y. Y.; Xu, L.; Zeng, Y.; Yu, J.; Zhang, W. Q.; Wang, L. et al. A dual chemodrug-loaded hyaluronan nanogel for differentiation induction therapy of refractory AML via disrupting lysosomal homeostasis. *Sci. Adv.* **2025**, *11*, eado3923.
[22] Luga, V.; Wrana, J. L. Tumor-stroma interaction: Revealing fibroblast-secreted exosomes as potent regulators of Wnt-planar cell polarity signaling in cancer metastasis. *Cancer Res.* **2013**, *73*, 6843–6847.
[23] Naser, R.; Fakhoury, I.; El-Fouani, A.; Abi-Habib, R.; El-Sibai, M. Role of the tumor microenvironment in cancer hallmarks and targeted therapy (review). *Int. J. Oncol.* **2023**, *62*, 23.
[24] Baghban, R.; Roshangar, L.; Jahanban-Esfahlan, R.; Seidi, K.; Ebrahimi-Kalan, A.; Jaymand, M.; Kolahian, S.; Javaheri, T.; Zare, P. Tumor microenvironment complexity and therapeutic implications at a glance. *Cell Commun. Signal.* **2020**, *18*, 59.
[25] Malla, R. R.; Kiran, P. Tumor microenvironment pathways: Cross regulation in breast cancer metastasis. *Genes Dis.* **2022**, *9*, 310–324.
[26] Kalluri, R. The biology and function of fibroblasts in cancer. *Nat. Rev. Cancer* **2016**, *16*, 582–598.
[27] Lavie, D.; Ben-Shmuel, A.; Erez, N.; Scherz-Shouval, R. Cancer-associated fibroblasts in the single-cell era. *Nat. Cancer* **2022**, *3*, 793–807.
[28] Wang, Y. B.; Gan, G. F.; Wang, B. C.; Wu, J. L.; Cao, Y.; Zhu, D.; Xu, Y.; Wang, X. N.; Han, H. X.; Li, X. L. et al. Cancer-associated fibroblasts promote irradiated cancer cell recovery through autophagy. *eBioMedicine* **2017**, *17*, 45–56.
[29] Sarkar, M.; Nguyen, T.; Gundre, E.; Ogunlusi, O.; El-Sobky, M.; Giri, B.; Sarkar, T. R. Cancer-associated fibroblasts: The chief architect in the tumor microenvironment. *Front. Cell Dev. Biol.* **2023**, *11*, 1089068.
[30] Glabman, R. A.; Choyke, P. L.; Sato, N. Cancer-associated fibroblasts: Tumorigenicity and targeting for cancer therapy. *Cancers (Basel)* **2022**, *14*, 3906.
[31] Fidler, I. J.; Ellis, L. M. The implications of angiogenesis for the biology and therapy of cancer metastasis. *Cell* **1994**, *79*, 185–188.
[32] Orimo, A.; Gupta, P. B.; Sgroi, D. C.; Arenzana-Seisdedos, F.; Delaunay, T.; Naeem, R.; Carey, V. J.; Richardson, A. L.; Weinberg, R. A. Stromal fibroblasts present in invasive human breast carcinomas promote tumor growth and angiogenesis through elevated SDF-1/CXCL12 secretion. *Cell* **2005**, *121*, 335–348.
[33] Weidner, N.; Carroll, P. R.; Flax, J.; Blumenfeld, W.; Folkman, J. Tumor angiogenesis correlates with metastasis in invasive prostate carcinoma. *Am. J. Pathol.* **1993**, *143*, 401–409.
[34] Ohashi, T.; Erickson, H. P. Revisiting the mystery of fibronectin multimers: The fibronectin matrix is composed of fibronectin dimers cross-linked by non-covalent bonds. *Matrix Biol.* **2009**, *28*, 170–175.
[35] Zerlauth, G.; Wolf, G. Plasma fibronectin as a marker for cancer and other diseases. *Am. J. Med.* **1984**, *77*, 685–689.
[36] Pankov, R.; Yamada, K. M. Fibronectin at a glance. *J. Cell Sci.* **2002**, *115*, 3861–3863.
[37] Huang, L.; Xu, A. M.; Liu, S.; Liu, W.; Li, T. J. Cancer-associated fibroblasts in digestive tumors. *World J. Gastroenterol.* **2014**, *20*, 17804–17818.
[38] Nurmik, M.; Ullmann, P.; Rodriguez, F.; Haan, S.; Letellier, E. In search of definitions: Cancer-associated fibroblasts and their markers. *Int. J. Cancer* **2020**, *146*, 895–905.
[39] Dai, J.; Ouyang, H. Z.; Wei, S. M.; Chen, B.; Dong, X. Y.; Hu, J. J.; Wu, M.; Wang, S. X.; Xia, F.; Lou, X. D. Cancer-associated fibroblast mimetic AIE probe for precision imaging-guided full-cycle management of ovarian cancer surgery. *Anal. Chem.* **2023**, *95*, 15068–15077.
[40] Knowles, L. M.; Malik, G.; Hood, B. L.; Conrads, T. P.; Pilch, J. CLT1 targets angiogenic endothelium through CLIC1 and fibronectin. *Angiogenesis* **2012**, *15*, 115–129
[41] Ye, F. R.; Jeong, E. K.; Parker, D.; Lu, Z. R. Evaluation of CLT1-(Gd-DTPA) for MR molecular imaging in a mouse breast cancer model. *Chin. J. Magn. Reson. Imaging* **2011**, *2*, 325–330.
[42] Ye, F. R.; Jeong, E. K.; Jia, Z. J.; Yang, T. X.; Parker, D.; Lu, Z. R. A peptide targeted contrast agent specific to fibrin-fibronectin complexes for cancer molecular imaging with MRI. *Bioconjug. Chem.* **2008**, *19*, 2300–2303.
[43] Pilch, J.; Brown, D. M.; Komatsu, M.; Järvinen, T. A. H.; Yang, M.; Peters, D.; Hoffman, R. M.; Ruoslahti, E. Peptides selected for binding to clotted plasma accumulate in tumor stroma and wounds. *Proc. Natl. Acad. Sci. USA* **2006**, *103*, 2800–2804.
[44] Zhang, B.; Shen, S.; Liao, Z. W.; Shi, W.; Wang, Y.; Zhao, J. J.; Hu, Y.; Yang, J. R.; Chen, J.; Mei, H. et al. Targeting fibronectins of glioma extracellular matrix by CLT1 peptide-conjugated nanoparticles. *Biomaterials* **2014**, *35*, 4088–4098.
[45] Zhang, L. L.; Sun, L. H.; Tang, Q. S.; Sun, S. H.; Zeng, L.; Ma, J. Y.; Li, X. D.; Ge, H. Y.; Liang, X. L. Cascade drug delivery through tumor barriers of pancreatic cancer via ultrasound in combination with functional microbubbles. *ACS Biomater. Sci. Eng.* **2022**, *8*, 1583–1595.
[46] Chen, X. H.; Jia, F.; Huang, Y.; Jin, Q.; Ji, J. Cancer-associated fibroblast-targeted delivery of captopril to overcome penetration obstacles for enhanced pancreatic cancer therapy. *ACS Appl. Bio Mater.* **2022**, *5*, 3544–3553.
[47] Zong, L. L.; Dai, Y. X.; Xu, J. H.; Qiao, C. F.; Qi, Y.; Ma, C. Y.; Li, H.; Pang, X. B.; Pu, X. H. Luteolin and glycyrrhetinic exert cooperative effect on liver cancer by selfassembling into carrier-free nanostructures. *Chin. Chem. Lett.* **2025**, *36*, 111325.
[48] Lang, J. Y.; Zhao, X.; Qi, Y. Q.; Zhang, Y. L.; Han, X. X.; Ding, Y. P.; Guan, J. J.; Ji, T. J.; Zhao, Y.; Nie, G. J. Reshaping prostate tumor microenvironment to suppress metastasis via cancer-associated fibroblast inactivation with peptide-assembly-based nanosystem. *ACS Nano* **2019**, *13*, 12357–12371.
[49] Xian, P.; Zou, L. H.; Zhang, J. X.; Pan, X. E.; Song, Y. J.; Nan, Y. R.; Pu, Q.; Liu, H. Z.; Green, D.; Ni, S. T. et al. Precision targeted cancer-associated fibroblast nano-regulator enhanced chemo-immunotherapy for triple-negative breast cancer. *Biomaterials* **2026**, *326*, 123679.
[50] Guo, D. X.; Ji, X. Y.; Xie, H.; Ma, J.; Xu, C. C.; Zhou, Y. F.; Chen, N.; Wang, H.; Fan, C. H.; Song, H. Y. Targeted reprogramming of vitamin B_3 metabolism as a nanotherapeutic strategy towards chemoresistant cancers. *Adv. Mater.* **2023**, *35*, 2301257.
[51] Qiu, Z. W.; Zhong, Y. T.; Lu, Z. M.; Yan, N.; Kong, R. J.; Huang, J.

Q.; Li, Z. F.; Nie, J. M.; Li, R. Q.; Cheng, H. Breaking physical barrier of fibrotic breast cancer for photodynamic immunotherapy by remodeling tumor extracellular matrix and reprogramming cancer-associated fibroblasts. *ACS Nano* **2024**, *18*, 9713–9735.

[52] Sharifi, N.; Gulley, J. L.; Dahut, W. L. Androgen deprivation therapy for prostate cancer. *JAMA* **2005**, *294*, 238–244.

[53] Farsaci, B.; Donahue, R. N.; Coplin, M. A.; Grenga, I.; Lepone, L. M.; Molinolo, A. A.; Hodge, J. W. Immune consequences of decreasing tumor vasculature with antiangiogenic tyrosine kinase inhibitors in combination with therapeutic vaccines. *Cancer Immunol. Res.* **2014**, *2*, 1090–1102.

[54] Wu, Y.; Xie, H. L.; Li, Y. P.; Bao, X. Y.; Lu, G. L.; Wen, J. Y.; Gao, Y.; Li, Y. P.; Zhang, Z. W. Nitric oxide-loaded bioinspired lipoprotein normalizes tumor vessels to improve intratumor delivery and chemotherapy of albumin-bound paclitaxel nanoparticles. *Nano Lett.* **2023**, *23*, 939–947.

[55] Ito, K.; Scott, S. A.; Cutler, S.; Dong, L. F.; Neuzil, J.; Blanchard, H.; Ralph, S. J. Thiodigalactoside inhibits murine cancers by concurrently blocking effects of galectin-1 on immune dysregulation, angiogenesis and protection against oxidative stress. *Angiogenesis* **2011**, *14*, 293–307.

[56] Xiang, T.; Lin, Y. X.; Ma, W. L.; Zhang, H. J.; Chen, K. M.; He, G. P.; Zhang, X.; Xu, M.; Feng, Q. S.; Chen, M. Y. et al. Vasculogenic mimicry formation in EBV-associated epithelial malignancies. *Nat. Commun.* **2018**, *9*, 5009.

[57] Henke, E.; Nandigama, R.; Ergün, S. Extracellular matrix in the tumor microenvironment and its impact on cancer therapy. *Front. Mol. Biosci.* **2020**, *6*, 160.

[58] Li, Y.; Li, L.; Qin, J.; Wu, J. Y.; Dai, X. M.; Xu, J. M. OSR1 phosphorylates the Smad2/3 linker region and induces TGF-beta1 autocrine to promote EMT and metastasis in breast cancer. *Oncogene* **2021**, *40*, 68–84.

[59] Huang, M. L.; Fu, M. R.; Wang, J.; Xia, C. H.; Zhang, H.; Xiong, Y. Q.; He, J. K.; Liu, J. M.; Liu, B. C.; Pan, S. Y. et al. TGF-β1-activated cancer-associated fibroblasts promote breast cancer invasion, metastasis and epithelial-mesenchymal transition by autophagy or overexpression of FAP-α. *Biochem. Pharmacol.* **2021**, *188*, 114527.

[60] Kamaly, N.; He, J. C.; Ausiello, D. A.; Farokhzad, O. C. Nanomedicines for renal disease: Current status and future applications. *Nat. Rev. Nephrol.* **2016**, *12*, 738–753.

[61] Zhao, C. R.; Li, J. Y.; Jiang, Z. T.; Zhu, J. J.; Zhao, J. N.; Yang, Q. R.; Yao, W. J.; Pang, W.; Li, N.; Yu, M. R. et al. Disturbed flow-facilitated margination and targeting of nanodisks protect against atherosclerosis. *Small* **2023**, *19*, 2204694.

[62] Oroojalian, F.; Charbgoo, F.; Hashemi, M.; Amani, A.; Yazdian-Robati, R.; Mokhtarzadeh, A.; Ramezani, M.; Hamblin, M. R. Recent advances in nanotechnology-based drug delivery systems for the kidney. *J. Control. Release* **2020**, *321*, 442–462.

[63] Peinado, H.; Zhang, H. Y.; Matei, I. R.; Costa-Silva, B.; Hoshino, A.; Rodrigues, G.; Psaila, B.; Kaplan, R. N.; Bromberg, J. F.; Kang, Y. B. et al. Pre-metastatic niches: Organ-specific homes for metastases. *Nat. Rev. Cancer* **2017**, *17*, 302–317.

[64] Moretti, F. A.; Chauhan, A. K.; Iaconcig, A.; Porro, F.; Baralle, F. E.; Muro, A. F. A major fraction of fibronectin present in the extracellular matrix of tissues is plasma-derived. *J. Biol. Chem.* **2007**, *282*, 28057–28062.

[65] Maurer, L. M.; Ma, W. J.; Mosher, D. F. Dynamic structure of plasma fibronectin. *Crit. Rev. Biochem. Mol. Biol.* **2016**, *51*, 213–227.

[66] Klotzsch, E.; Smith, M. L.; Kubow, K. E.; Muntwyler, S.; Little, W. C.; Beyeler, F.; Gourdon, D.; Nelson, B. J.; Vogel, V. Fibronectin forms the most extensible biological fibers displaying switchable force-exposed cryptic binding sites. *Proc. Natl. Acad. Sci. USA* **2009**, *106*, 18267–18272.

[67] Zou, Y. J.; Wang, Y. F.; Wen, X. H.; Li, C. H.; Lei, L.; Guo, Q. P.; Sun, G. M.; Yu, L.; Nie, H. M. A DNA aptamer targeting cellular fibronectin rather than plasma fibronectin for bioimaging and targeted chemotherapy of tumors. *Adv. Funct. Mater.* **2022**, *32*, 2205002.